- 1 Performance optimization and entropy-TOPSIS
- 2 evaluation of a thermochemical solar thermal power
- 3 generation system based on packed bed reactor
- 4 exothermic characteristics
- 5 Jianing Chen ^a, Xueming Yang ^{a*}, Jie Cui ^a, Yinqiao Huo ^a, Jianfei Xie ^b
- ^a Hebei Key Laboratory of Low Carbon and High Efficiency Power Generation Technology,
- 7 Department of Power Engineering, North China Electric Power University, Baoding 071003,
- 8 P. R. China

- ⁹ School of Engineering, University of Derby, DE22 3AW, United Kingdom
- * Corresponding authors: xuemingyang@ncepu.edu.cn (X.M. Yang)

Abstract

12

13

14

15

16

17

18

19

20

21

22

23

24

25

26

27

28

29

30

31

32

33

34

37

38

39

40

41

Solar thermal power generation technology has enormous potential in global low-carbon energy transition, but its large-scale development is still constrained by solar intermittency and system stability issues. This study focuses on diatomite-modified calcium-based materials, revealing that diatomite modification transforms the exothermic reaction mechanism from an A3 model to a D2 model, significantly reducing activation energy by 8.69% and increasing the pre-exponential factor by 18.19%. The exothermic process in packed bed reactors was thoroughly investigated, illustrating the evolution patterns of temperature field, reaction extent, and pressure field. An innovative design incorporating intermediate air pathways was proposed, reducing reaction time by 28.57%. A novel thermochemical solar thermal power generation (TSTPG) system was established to systematically examine its performance from the perspective of reactor heat release characteristics. Through a comprehensive 4E (energy, exergy, economy, and environment) analysis framework, the mechanism of reactor parameter optimization on system energy efficiency improvement, exergy loss reduction, CO₂ emission reduction, and economic benefits was systematically investigated. A multi-dimensional evaluation methodology based on entropy-TOPSIS (Technique for Order Preference by Similarity to Ideal Solution) was proposed, incorporating power generation capacity, energy efficiency, exergy efficiency, annual total cost, and carbon emission reduction. Results demonstrate that the newly established system achieved impressive energy and exergy efficiencies of 56.86% and 49.06% respectively under optimal conditions (650 K), along with power generation of 48.31 MWh and a total annual cost of 4.11 m\$/year, showing promising prospects for engineering applications.

35 **Keyword:** Thermochemical energy storage; Packed bed reactor; Solar thermal power generation system; 4E analysis; Entropy-TOPSIS method

1. Introduction

With the intensifying global energy crisis and environmental issues, the development and utilization of renewable energy has gained increasing attention. Solar energy, with its characteristics of being clean, renewable, and abundant, holds a significant position in future energy systems^[1]. However, the intermittency and instability of solar energy severely restrict

its large-scale application, primarily manifested in the supply-demand mismatch caused by diurnal and seasonal variations. Therefore, developing efficient energy storage technologies is crucial for improving the solar energy utilization efficiency and achieving a stable energy supply^[2].

Currently, solar thermal power generation systems mainly employ the sensible heat and latent heat storage technologies^[3]. Among these, molten salt as a heat storage medium has achieved commercial applications, as demonstrated in Spain's Gemasolar plant^[4] and the United States' Crescent Dunes plant^[5]. However, molten salt storage systems face several challenges: high melting point requires a continuous heating to prevent solidification; strong corrosiveness happens to the equipment; low energy storage density requires large storage tanks. In addition, heat loss during the storage process significantly affects the system's long-term performance^[6]. In comparison, thermochemical energy storage (TCES) based on the CaCO₃/CaO system offers advantages such as high energy storage density^[7], long storage duration, and negligible heat loss during storage^[8]. The reaction can be expressed as:

$$\begin{array}{ccc}
\operatorname{CaCO}_{3} f & \operatorname{CaO} + \operatorname{CO}_{2} \\
\Delta H = 177.9 \text{kJ/mol}
\end{array} \tag{1}$$

Calcium-based materials face issues of sintering and poor reaction kinetics during cycling, which seriously affect their practical applications. Therefore, material modification is necessary to improve the cycling stability and reaction kinetics^[9]. For TCES reactors, chemical reactivity and heat/mass transfer performance are primary factors. To address this, researchers have designed and studied various reactor structures^[10]. At the system integration level, the calcium cycle (CaL) process is typically coupled with concentrated solar power (CSP) systems to form Cal-CSP systems. To optimize system performance, researchers also have proposed various innovative system configurations and operational strategies to evaluate the system performance through different efficiency indicators^[11].

As mentioned above, researchers have used the inert oxide doping to improve the cycling stability and mitigate the degradation of thermal storage density, including Al₂O₃^[12], SiO₂^[13], TiO₂ ^[14], MgO^[15], etc. TCES reactors play a key role in the system. Packed bed reactors offer advantages such as low cost, ease of operation, and easy control of operating parameters. Xu et al.^[14] achieved efficient thermal storage performance of the CaO/CaCO₃

system in their developed fixed-bed thermochemical reactor, achieving a maximum temperature difference of 309.83°C at an operating temperature of 550°C and reaching a maximum absolute temperature of 848.7°C at 750°C, maintaining 27.72% of the reaction time within 800-900°C. Deng et al.[16] studied the exothermic process of CaCO₃/CaO thermochemical reactors and found that considering CO₂ flow could increase the reaction rate by 16.23%, while increasing the reactor thermal conductivity (from 1.33 W/m·K to 4 W/m·K) could improve the reaction rate by 60.26%. Adding cooling channels in the reactor could further optimize the heat transfer performance, increasing the reaction rate by 34.94%. Tian et al.^[17] comprehensively evaluated the thermochemical energy storage performance of the CaCO₃/CaO system in a fixed-bed reactor. Experimental results showed that CaCO₃ decomposition conversion reached 63.8% at 850°C, which was followed by CaO carbonation conversion of 67.2% at 750°C. Reducing bed packing density could improve the storage efficiency but would decrease the heat release. Further numerical simulations explored the influence of key operating parameters, finding that calcination temperature (800-950°C) and material porosity (0.6-0.7) were the main factors which affected the system performance. Higher temperatures could increase decomposition conversion from 37.6% to 92.6%, while appropriate porosity could balance the gas diffusion and heat transfer efficiency.

In 1980s, Barker^[18] proposed the CaL process, which forms the foundation of CSP plant designs. Chen et al.^[19] developed a novel CaL-based solar thermochemical energy storage power plant system, which can be working in both day and night modes, avoiding the drawback of 24-hour continuous carbonation. The system achieved a global storage efficiency of 37.60% and a global power generation efficiency of 48.04%, surpassing the existing system's 45% power generation efficiency level, while requiring about 33% less CaO (reduced from 680 tons to 453 tons) compared to traditional systems. Ortiz et al.^[20] developed a novel CaL-based high-temperature storage solar combined cycle system by integrating the solar receiver-calcium looping storage-CO₂ Brayton cycle. The system could achieve an overall system efficiency of 44.5% under design conditions. Operating in different modes during day or night at high temperatures of 1000°C, it could achieve 12 hours of full-load power generation daily, showing significant improvement over the existing integrated solar combined cycle power plants (ISCC) with 20% solar share. Zhang et al.^[11] developed a solar-

thermochemical energy storage based trigeneration system using CaL process as storage medium, whether operating in day or night mode, capable of producing 2618.09 MW of electricity, 305.56 MW of heating, and 523.88 MW of cooling capacity daily. Results showed that the system's total energy efficiency and total exergy efficiency could reach 56.92% and 35.94% respectively, while reducing 2222.76 tons of CO₂ emissions and 696.41 m³ of fossil fuel consumption daily. Ahmad et al. [21] analyzed the performance of three different cooling systems for solar panels (single-pass duct, multi-pass duct, and tube-type heat absorber) based on the climatic conditions of Islamabad, Pakistan, with results indicating that the multipass duct design was most effective. This optimized design, utilizing 31 passes, achieved a maximum power output of 186.713W at a water flow rate of 0.14 kg/s while maintaining the panel temperature at 38.81°C, significantly enhancing system efficiency. Sher et al. [22] investigated the effects of various environmental factors on photovoltaic performance, demonstrating that dust accumulation (particularly ash particles) significantly reduces solar panel efficiency, with experimental results showing efficiency decreases of up to 94.3% with 121 g/m² of ash compared to clean panels. Their research further established that relative humidity above 50% negatively impacts performance, though this effect is less pronounced at higher light intensities, providing valuable insights for optimizing solar energy systems in challenging environmental conditions.

Although significant progress has been made in thermochemical energy storage systems, previous studies have mainly focused on material modification and system integration, lacking systematic investigations of the exothermic process at the reactor level. Chen et al. [7] examined the heat storage process of diatomite-doped calcium-based materials, but the energy exothermic process, which directly affects power generation efficiency and economics, remains insufficiently researched. The main objective of this study is to systematically investigate the application of diatomite-modified calcium-based materials in solar thermochemical energy storage systems, spanning from reaction kinetics to system-level performance. Unlike previous studies that focus solely on individual aspects (materials, reactors, or systems), we reveal the intrinsic connections between material modification, reactor parameters, and system performance. Specifically, this research aims to: (1) characterize the effect of diatomite modification on exothermic reaction mechanisms, (2)

analyze the evolution patterns and performance factors in packed bed reactor exothermic processes, and (3) establish and evaluate a novel thermochemical solar thermal power generation (TSTPG, as shown in Fig.1) system through comprehensive 4E analysis and entropy-TOPSIS multi-dimensional evaluation.

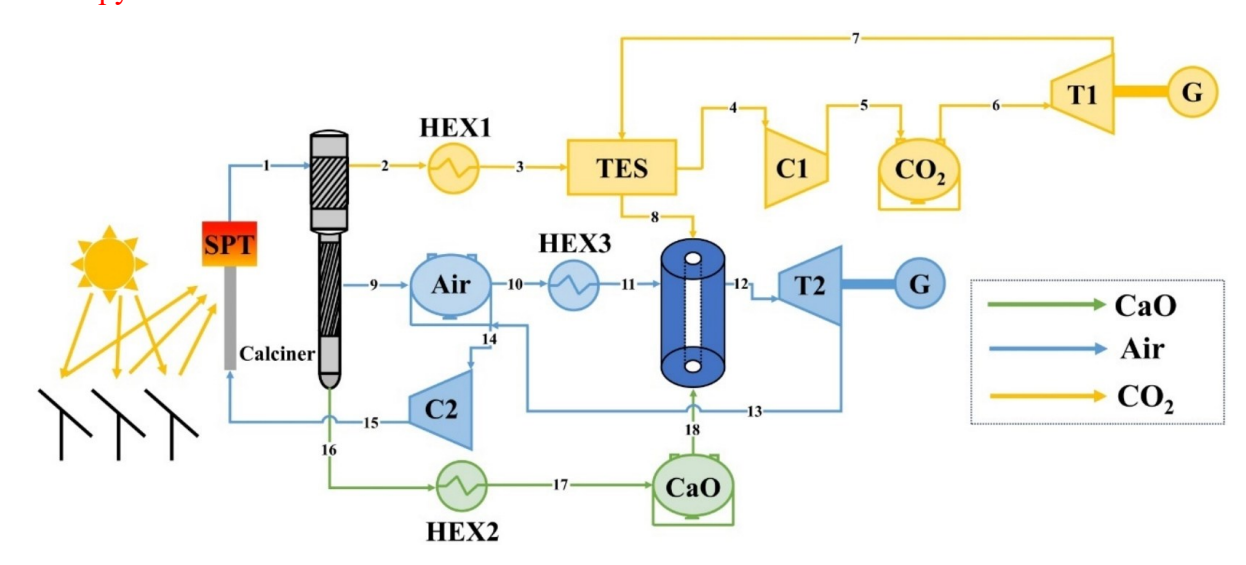


Fig. 1 Schematic of thermochemical solar thermal power generation (TSTPG) system.

2. Numerical method

2.1 Kinetics of the SCAM exothermic reaction

Details about the preparation, cycling stability, and heat storage reaction kinetics of pure calcium carbonate material (PCAM) and calcium-based heat storage material doped with diatomite (SCAM) were discussed in our previous research^[7]. This study is only focused on the establishment of the exothermic reaction kinetics of PCAM and SCAM.

In this study, TGA thermogravimetric curves were used to analyze the reaction kinetics and provide parameters for optimizing the thermochemical exothermic reactor. The Coats-Redfern (C-R) integral method and the Archar-Brindly-Sharp-Wendworth (ABSW) differential method were applied to determine these parameters^[23].

Eq. (2) can be used to describe the ABSW method:

$$\ln\left(\frac{\mathrm{d}(\alpha)}{f(\alpha)\mathrm{d}T}\right) = \ln\left(\frac{A}{\beta}\right) - \frac{E}{RT} \tag{2}$$

Eq. (3) can be used to describe the C-R method:

$$\ln\left(\frac{g(\alpha)}{T^2}\right) = \ln\left(\frac{AR}{\beta E}\right) - \frac{E}{RT} \tag{3}$$

$$\alpha = \frac{\Delta m}{\Delta m_o} \tag{4}$$

where A is the pre-exponential factor, R is the gas constant of 8.314 J/(mol·K), E is the activation energy of the reaction in kJ/mol, β is the heating rate of 15 K/min, T is the reaction temperature in K, α is the reaction extent coefficient ranging from 0 to 1, Δm is the current weight gain, Δm_o is the total weight gain, $f(\alpha)$ and $g(\alpha)$ are the reaction kinetics mechanism functions for ABSW differential method and C-R integral method respectively. Table 1 shows different kinetic mechanism models.

Table 1-Various exothermic kinetic mechanism models.

Mechanism function	Symbols	$f(\alpha)$	$g(\alpha)$
Avrami-Erofeev	A2	$2[-\ln(1-\alpha)]^{1/2}(1-\alpha)$	$[-\ln(1-\alpha)]^{1/2}$
Avrami-Erofeev	A3	$3[-\ln(1-\alpha)]^{1/3}(1-\alpha)$	$[-\ln(1-\alpha)]^{1/3}$
Avrami-Erofeev	A4	$4[-\ln(1-\alpha)]^{1/4}(1-\alpha)$	$[-\ln(1-\alpha)]^{1/4}$
Contracting cylinder	R2	$2(1-\alpha)^{1/2}$	$1-(1-\alpha)^{1/2}$
Contracting sphere	R3	$3(1-\alpha)^{2/3}$	$1-(1-\alpha)^{1/3}$
1-dimensional diffusion	D1	$(1/2) \alpha^{-1}$	α^2
2-dimensional diffusion	D2	$[-\ln(1-\alpha)]^{-1}$	$(1-\alpha)\ln(1-\alpha)+\alpha$
3-dimensional diffusion	D3	$3/2(1-\alpha)^{2/3}[1-(1-\alpha)^{1/3}]^{-1}$	$(1-(1-\alpha)^{1/3})^2$

To obtain reasonable kinetic models $f(\alpha)$ and $g(\alpha)$, the maximum Rs method is applied to Eqs. (2) and (3). Figs. 2 and 3 show the models obtained by fitting the thermogravimetric curves using the ABSW differential method and C-R integral method in PCAM and SCAM, respectively. Tables 2 and 3 display the Rs values obtained from the fitting calculations using the ABSW differential method and C-R integral method. The A3 model with the highest confidence level is selected in PCAM, and the D2 model with the highest confidence level is chosen in SCAM.

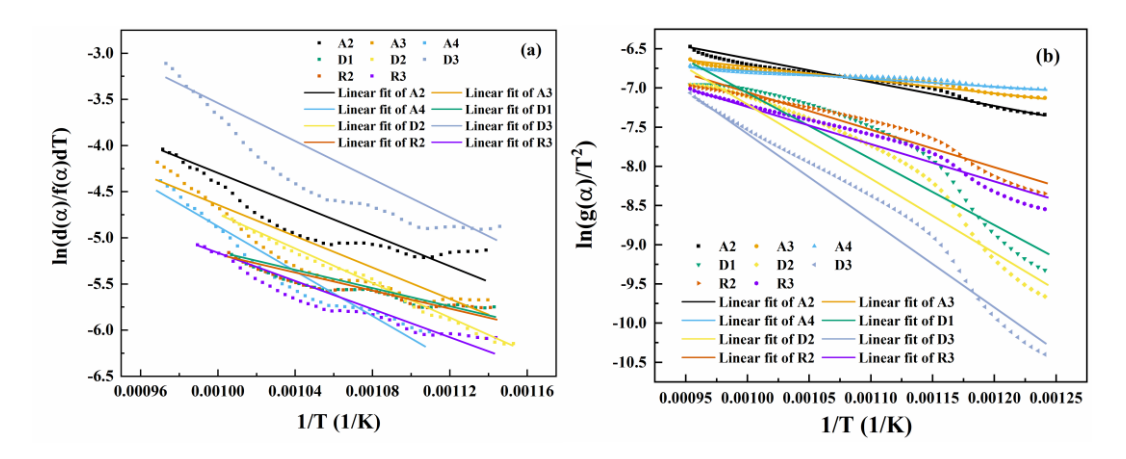


Fig. 2 Various exothermic kinetic mechanism models of PCAM: (a) ABSW difference method and (b) C-R integral method.

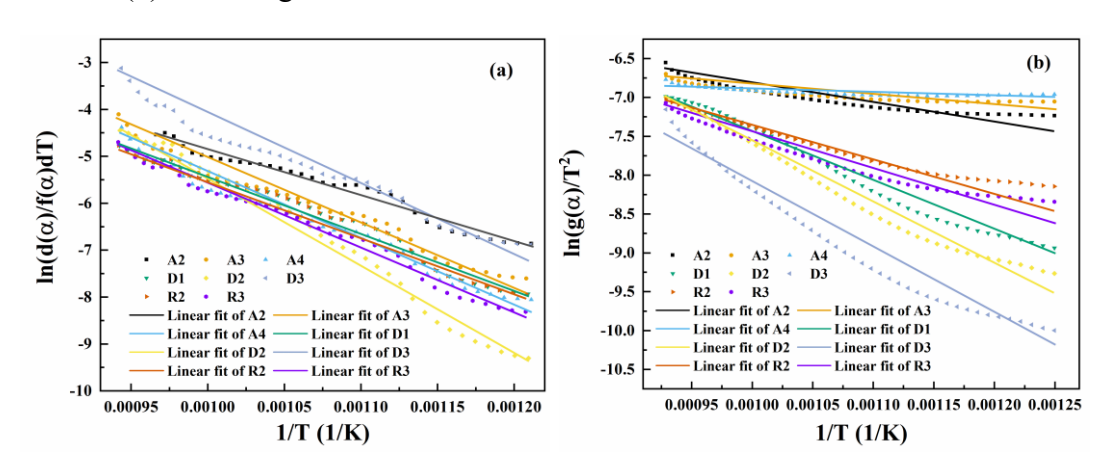


Fig. 3 Various exothermic kinetic mechanism models of SCAM: (a) ABSW difference method and (b) C-R integral method.

172 Table 2- Rs of the PCAM exothermic kinetics mechanism function.

166

167

168

169

170

Mechanism function	A2	A3	A4	D1	D2	D3	R2	R3
Rs(ABSW difference method)	0.8390	0.8899	0.9373	0.9071	0.9944	0.8840	0.9095	0.9258
$Rs_{(C-R integral method)}$	0.9758	0.9639	0.9417	0.8915	0.9288	0.9692	0.9427	0.9627
Rs(Average)	0.9074	0.9629	0.9395	0.8993	0.9616	0.9266	0.9261	0.9443

173 Table 3- Rs of the SCAM exothermic kinetics mechanism function.

Mechanism function	A2	A3	A4	D1	D2	D3	R2	R3
Rs _{(ABSW} difference method)	0.9721	0.9799	0.9827	0.9795	0.9904	0.9774	0.9794	0.9880

Rs(C-R integral method)	0.9044	0.8485	0.7227	0.9867	0.9820	0.9675	0.9707	0.9615
Rs(Average)	0.9383	0.9142	0.8527	0.9831	0.9862	0.9723	0.9751	0.9748

The pre-exponential factor A and activation energy E of the exothermic reaction kinetic equation can be calculated by fitting the intercept and slope of the curve, respectively, according to Eqs. (2) and (3). Table 4 presents the pre-exponential factor and activation energy for PCAM and SCAM. The corresponding exothermic reaction kinetics are described by Eqs. (5) and (6). The results for PCAM are consistent with the values reported in the literature^[24], demonstrating good reliability and consistency. The exothermic activation energy of the calcium-based material doped with diatomite was decreased from 74.74 kJ/mol to 68.22 kJ/mol, while the pre-exponential factor was increased from 162.88 s⁻¹ to 192.50 s⁻¹. This indicates that doping diatomite into calcium-based materials reduces the energy barrier required for the exothermic process, significantly enlarge the frequency factor for reaction initiation, thereby promoting the reaction and enhancing the material's exothermic reaction efficiency. The findings in this study are crucial for optimizing exothermic processes while designing the subsequent reactors.

Table 4- Exothermic reaction kinetic parameters of PCAM and SCAM.

C	ABSW diffe	rence method	C-R integra	ation method	Averaş	ge value
Group	E	A	E	A	E	A
PCAM	75.97	165.13	73.44	160.62	74.71	162.88
SCAM	70.16	194.23	66.28	190.76	68.22	192.50

$$\frac{d(\alpha)}{dt} = \frac{162.88}{\beta} \times \exp\left(\frac{-74.71}{RT}\right) \times 3\left[-\ln(1-\alpha)\right]^{1/3} (1-\alpha)$$
 (5)

$$\frac{d(\alpha)}{dt} = \frac{192.50}{\beta} \times \exp\left(\frac{-68.22}{RT}\right) \times \left[-\ln(1-\alpha)\right]^{-1}$$
 (6)

2.2. Reactor numerical simulation

The three-dimensional cylindrical packed bed reactor studied in this paper has been previously investigated in the heat storage process^[7]. It has a total height H of 600 mm, diameter D of 200 mm, and internal circular hole diameter D₁ of 40 mm, as shown in Fig. 4. During the exothermic process, CO₂ (reaction gas) flows into the reactor from the bottom

surface, initiating the carbonation reaction. High-temperature HTF (air) flows along the reactor outer wall to take away heat. To accurately study the exothermic process inside the reactor, 6 monitoring points were selected, with coordinates as shown in Fig. 4. The reactor is filled with SCAM, and the following assumptions are made to simplify the physics and chemical models of the exothermic process:

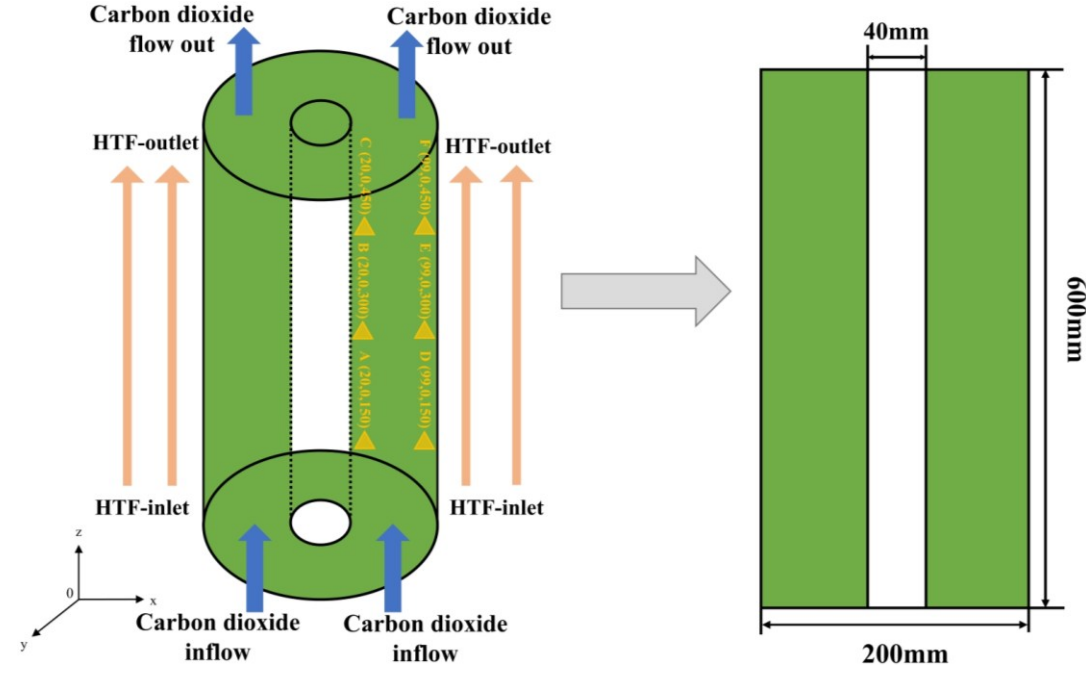


Fig. 4 Schematic illustration of a cylindrical packed bed reactor.

- 202 (1) The reactants in the reactor are treated as a continuous medium.
- 203 (2) The thermal conductivity, particle size, and porosity of solid reactants remain uniform 204 and constant during the exothermic process.
- 205 (3) Local thermal equilibrium is assumed for porous media, and radiation heat transfer is neglected.
- 207 (4) The gas phase is considered as an ideal gas.

195

196

197

198

199

- 208 (5) The exothermic process of reactants does not distinguish between kinetic control stage 209 and diffusion control stage.
- 210 (6) Based on previous experimental studies, the reaction is considered complete when the reaction extent reaches 0.85^[7].
- According to the previous work^[7], the relationship between the equilibrium pressure and temperature is shown as:

$$\ln\left(\frac{P}{100000}\right) = 23.6 - \frac{21397}{T_{eq}} \tag{7}$$

215 The change in reaction extent *X* during the exothermic process is expressed as:

$$\frac{\partial X}{\partial t} = K \tag{8}$$

- The reactants follow the law of mass conservation, and the mass conservation equation
- 218 for CO₂ entering the reactor is:

$$\frac{\partial}{\partial t} \left(\varepsilon_p \rho \right) + \nabla \cdot (\rho u) = Q_{\rm m} \tag{9}$$

- where u is the velocity of CO₂ gas. Darcy's law is used to couple the relationship between
- pressure field and velocity field^[25]:

$$k = \frac{D_p^2 \varepsilon^3}{180(1-\varepsilon)^2} \tag{11}$$

- where D_p is the particle size of the reactant.
- $Q_{\rm m}$ represents the mass source of the exothermic reaction, indicating the consumption
- of CO₂ or the amount of CO₂ absorbed by the reactant, expressed as:

$$Q_{\rm m} = \pm (1 - \varepsilon) \cdot f \cdot \Delta \rho \cdot \frac{dX}{dt} \tag{12}$$

The energy conservation equation is expressed as:

$$\frac{\partial ((\rho c_{p})_{\text{eff}} T)}{\partial t} + u \nabla ((\rho c_{p})_{g} T) = \nabla (\lambda_{\text{eff}} \nabla T) + Q_{h}$$
(13)

- where the energy source term Q_h (W·m⁻³) is related to the exothermic reaction in the porous
- reaction zone. It can be given below

$$Q_{\rm h} = \Delta H \cdot R \tag{14}$$

- The effective specific heat capacity is calculated by considering the conversion rates of
- reactants and products. The related physical parameters are shown as follows^[7]:

$$(\rho C_P)_{\text{eff}} = 0.63 \cdot (\varepsilon (\rho C_P)_{CO_2} + (1 - \varepsilon)(\rho C_P)_{solid}) + 0.37 \cdot (1 - \varepsilon) \cdot (\rho C_P)_{SiO_2}$$
(15)

$$\lambda_{\text{eff}} = 0.63 \cdot \left(\varepsilon \lambda_{CO_2} + (1 - \varepsilon) \lambda_{solid} \right) + 0.37 \cdot (1 - \varepsilon) \cdot \lambda_{SiO_2}$$
 (16)

237 The heat capacity and density of reactants and products are shown as:

$$c_{P,solid} = 0.63 \cdot \left((1 - X)c_{P,CaO} + Xc_{P,CaCO_3} \right) + 0.37 \cdot c_{P,SiO_2}$$
(17)

239
$$\rho_{solid} = 0.63 \cdot \left((1 - X) \rho_{CaO} + X \rho_{CaCO_3} \right) + 0.37 \cdot \rho_{SiO_3}$$
 (18)

- Air enters the HTF channel from the bottom and exchanges heat with the reactant. When 240
- the temperature rises, heat is taken away by air from the outlet: 241

$$(\rho c_{\rm p})_{\rm HTF} \frac{\partial T_{\rm HTF}}{\partial t} + (\rho c_{\rm p})_{\rm HTF} u_{\rm HTF} \cdot \nabla T_{\rm HTF} + \nabla \cdot q_{\rm HTF} = Q_{\rm HTF}$$
(19)

- 243 Through convective heat transfer, heat is transferred from the heat exchange wall to the
- flowing low-temperature fluid, effectively taking heat away from the reactor: 244

$$Q_{\rm HTF} = h_{\rm wall} \bullet (T - T_{\rm HTF}) \tag{20}$$

- 246 The Nusselt correlation is used to determine the heat transfer between HTF and the wall,
- and the heat transfer coefficient is defined by [26, 27]: 247

$$h_{\text{wall}} = \frac{\lambda \cdot Nu}{D} \tag{21}$$

- where D is the diameter of the HTF channel, and the Nusselt number is obtained through 249
- empirical formulas^[26, 27]: 250

$$Nu = 0.027 \cdot Re^{0.8} \cdot Pr^{0.3} \cdot \left(\frac{\mu}{\mu_{\text{wall T}}}\right)^{0.14}$$
 (22)

- Based on the above physics and chemical models, the values of important variables in 252 the Eqs are shown in Table 5^[7]. This study uses COMSOL software to simulate the 253 254 exothermic process. The initial and boundary conditions for the baseline case are listed in Table 6. The simulation model was validated by comparing the CaCO₃ exothermic process 255 with experimental results from Tian et al.[17], as shown in Fig. 5(a). The good agreement 256 257 between the simulation and experimental results showcases the model's reliability for the subsequent analysis of the packed bed reactor's exothermic performance. Fig. 5(b) shows the 258 grid independence verification results of this study. Models with grid numbers of 54,814, 259 119,383, 200,628, 257,592, and 500,039 were simulated under the baseline case. The analysis 260 261 revealed that the tetrahedral grid consisting of 257,592 provides optimal spatial resolution to
- accurately capture the essential thermochemical phenomena while maintaining 262
- 263 computational efficiency. Comparative evaluation demonstrated that the discrepancy in

predicted reaction time between this optimized mesh and the high-density configuration (500,039 grid) was negligible, conclusively validating the grid independence of the numerical solution.

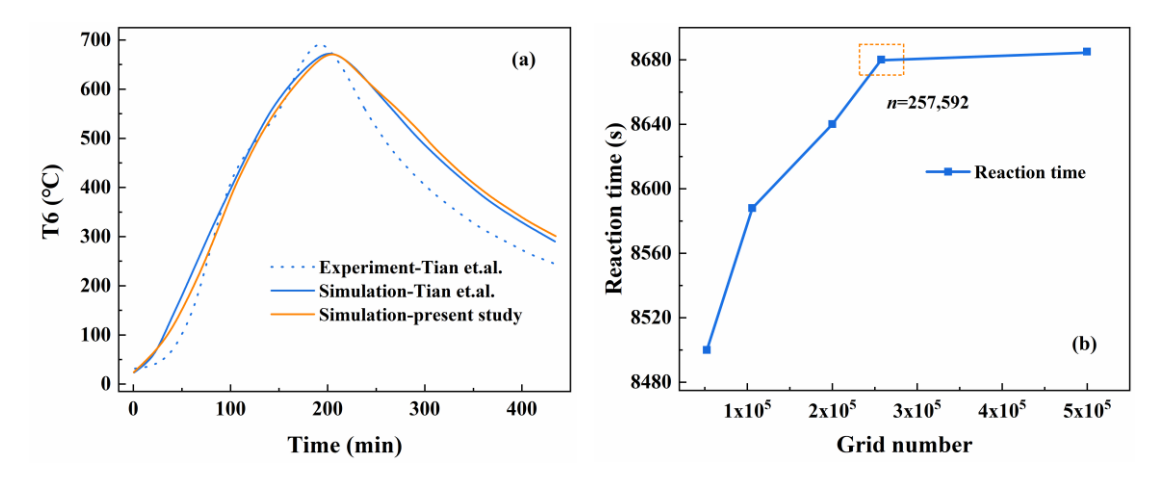


Fig. 5 (a) Validation of model results and (b) Grid independence verification.

269 Table 5- Thermophysical properties in the simulation.

Symbol	Parameter	Value
$M_{{\it CO}_2}$	Mole mass of CO ₂	44 g mol ⁻¹
M_{CaCO_3}	Mole mass of CaCO ₃	100 g mol ⁻¹
$M_{\it CaO}$	Mole mass of CaO	56 g mol ⁻¹
$ ho_{ extit{ iny CaCO}_3}$	Density of CaCO ₃	2.93 g cm ⁻³
$ ho_{{\it CaO}}$	Density of CaO	3.35 g cm^{-3}
$ ho_{{\scriptscriptstyle SiO_2}}$	Density of SiO ₂	2.2 g cm ⁻³
C_{CaCO_3}	Specific heat capacity of CaCO ₃	910 J kg ⁻¹ K ⁻¹
$C_{\it CaO}$	Specific heat capacity of CaO	799.1 J kg ⁻¹ K ⁻¹
$C_{{\scriptscriptstyle SiO_2}}$	Specific heat capacity of SiO ₂	703 J kg ⁻¹ K ⁻¹
λ_{solid}	Thermal conductivity of solid reactant	1.33 W m ⁻¹ K ⁻¹
A	Pre-exponential factor	192.50 s ⁻¹
E	Activation energy	68.22×10 ³ J mol ⁻¹

_
 ٠.
•

271

272

273

274

275

276

277

278

279

Porosity of reactant

0.6

Table 6- Initial and boundary conditions in the baseline case.

Initial/boundary conditions	Descriptions
$T_{\text{reactor}}(x, y, z, t = 0) = T_{\text{CO2_inlet}} = 700 \text{ K}$	Initial reactor temperature and CO ₂ inlet temperature
$T_{\rm HTF_inlet} = 700 \text{ K}$	Initial temperature of the HTF inlet
$V_{CO_2}^{\&}(x, y, 0, t = 0) = 10 \text{ L/min}, u_{HTF}(x, y, 0, t = 0) = 5 \text{ m/s}$	CO ₂ volumetric flow rate and initial velocity at the HTF inlet
$P(x, y, z, t = 0) = P_{\text{ini}} = 1 \text{ bar}$	Initial pressure inside the reactor
$u_{\text{wall}}(x, y, z, t) = 0$	No-slip velocity inside the HTF channel

2.3 SCAM TSTPG system simulation method

- Fig. 1 shows the process flow of the SCAM TSTPG system. Through solar heating of the thermochemical reactor designed in Section 2.2, SCAM decomposes into calcium oxide and carbon dioxide, where calcium oxide stores the absorbed heat, while the high-temperature carbon dioxide stores part of the heat through heat exchangers and drives the expander for power generation when needed. During peak electricity demand periods, when calcium oxide in the reactor reacts with carbon dioxide to release heat, the air system stores energy through convective heat transfer and compression processes, subsequently driving the expander for power generation during the expansion phase.
- The following assumptions are made for the TSTPG system:
- 281 (1) All components operate under steady-state conditions.
- 282 (2) Pipeline pressure drops are neglected.
- 283 (3) Except for the solar receiver and gas storage tanks (98% thermal insulation efficiency), all other components operate under adiabatic conditions.
- 285 (4) All compressors and expanders have constant isentropic efficiency, with power losses of 15%.
- 287 (5) Exergy analysis is performed at an environmental temperature of 25°C and a pressure of 1.01 bar. while pump power consumption is neglected.
- In this study, energy and exergy analyses are conducted for key components, and the energy and exergy balances of various components are shown in Tables 7 and 8.

	able / -1 ne energy balance of the components.	
Component	Energy Balance Peak electrical load mode	Low electrical load mode
SPT	$\mathcal{O}_{SPT}^{\mathbf{x}} = n^{\mathbf{x}}_{\mathbf{x}}h_{1} - n^{\mathbf{x}}_{\mathbf{x}_{5}}h_{15}$	
Reactor	$\mathcal{E}_{react_heat} = n \mathcal{E}_{cao} c_{cao} \left(\sum_{product} X h_{product} - \sum_{react} X h_{react} \right)$	$\mathcal{E}_{react_heat} = n \mathcal{E}_{caco3} c_{caco3} \left(\sum_{product} X h_{product} - \sum_{react} X h_{react} \right)$
HEX1	$\mathcal{G}_{HEX1}^{\mathcal{E}} = n_{2}^{\mathcal{E}} h_{2} - n_{3}^{\mathcal{E}} h_{3}$	
TES	$Q_{TES}^{2} = n S_{5}h_{3} - n S_{4}h_{4} = n S_{6}h_{8} - n S_{7}h_{7}$	
C1		$W_{C1}^{\mathcal{G}} = (n\mathcal{S}_5 h_5 - n\mathcal{S}_4 h_4) \cdot \eta_c$
T1	$N_{T_1}^{\mathbf{x}} = (n_{\mathbf{x}}^{\mathbf{x}} h_6 - n_{\mathbf{x}}^{\mathbf{x}} h_7) \cdot \eta_t$	
CO _{2storage}	$n \xi_5 h_5 = n \xi_5 h_6$	
Air _{storage}	$n_{5}^{2}h_{9}=n_{10}^{2}h_{10}$	
HEX3	$\mathcal{G}_{HEX3}^{k} = n k_0 h_{10} - n k_1 h_{11}$	
C2		$W_{C2}^{8c} = (n_{15}^{8c}h_{15} - n_{14}^{8c}h_{14}) \cdot \eta_{c}$
T2	$W_{T2}^{\&} = (n_{12}^{\&}h_{12} - n_{13}^{\&}h_{13}) \cdot \eta_{t}$	
HEX2	$Q_{HEX2}^{c} = n k_{16} h_{16} - n k_{17} h_{17}$	
CaO _{storage}	$n_{17}^{8}h_{17} = n_{18}^{8}h_{18}$	
292 Ta	able 8-The exergy balance of the components.	
Component	Exergy Balance Peak electrical load mode	Low electrical load mode
SPT	$\mathbf{E}_{SPT,f}^{\mathbf{X}} + \mathbf{E}_{\mathbf{X}_{15}}^{\mathbf{X}} = \mathbf{E}_{\mathbf{X}_{1}}^{\mathbf{X}} - \mathbf{E}_{\mathbf{X}_{SPT,floss}}^{\mathbf{X}}$	
Reactor	$EX_{11} + EX_{18} + EX_{8} + EX_{CaO} = EX_{12} + EX_{CaOloss}$	$E_{X_1}^{A} + E_{X_{CaCO_3}}^{A} = E_{X_2}^{A} + E_{X_9}^{A} + E_{X_{16}}^{A} + E_{X_{CaCO_3loss}}^{A}$

Reactor
$$\cancel{E}X_{11} + \cancel{E}X_{18} + \cancel{E}X_{8} + \cancel{E}X_{CaO} = \cancel{E}X_{12} + \cancel{E}X_{CaOloss}$$
 $\cancel{E}X_{1} + \cancel{E}X_{CaCO_3} = \cancel{E}X_{2} + \cancel{E}X_{9} + \cancel{E}X_{16} + \cancel{E}X_{CaCO_3loss}$

HEX1 $\cancel{E}X_{2} = \cancel{E}X_{3} + \cancel{E}X_{HEX1} + \cancel{E}X_{HEX1loss}$

TES $\cancel{E}X_{7} + \cancel{E}X_{3} + \cancel{E}X_{TES} = \cancel{E}X_{4} + \cancel{E}X_{8} + \cancel{E}X_{TESloss}$

C1 $\cancel{E}X_{4} + \cancel{W}_{C1} = \cancel{E}X_{5} + \cancel{E}X_{Clloss}$

T1
$$E_{X_6}^{A} = E_{X_7}^{A} + W_{T1}^{A} + E_{X_{T1loss}}^{A}$$

CO_{2storage} $E_{X_5}^{A} = E_{X_6}^{A}$

Air_{storage} $E_{X_9}^{A} = E_{X_{10}}^{A}$

HEX3 $E_{X_{10}}^{A} = E_{X_{11}}^{A} + E_{X_{HEX3}}^{A} + E_{X_{HEX3loss}}^{A}$

C2 $E_{X_{12}}^{A} = E_{X_{13}}^{A} + E_{X_{T2loss}}^{A} + W_{T2}^{A}$

HEX2 $E_{X_{16}}^{A} = E_{X_{17}}^{A} + E_{X_{HEX2}}^{A} + E_{X_{HEX2loss}}^{A}$

CaO_{storage} $E_{X_{17}}^{A} = E_{X_{18}}^{A}$

The fuel exergy of SPT can be determined below [28].

$$\mathcal{E}_{SPT,f} = DNI \cdot A_{mirror} \left(1 - \frac{T_0}{T_{sun}} \right)$$
 (23)

2.3.1 Solar power tower (SPT)

The SPT consists of mirrors and a receiver, and mirrors concentrate solar radiation onto the receiver at the tower top. This increases the HTF temperature while experiencing convective and radiative heat losses. Following the receiver passage, HTF enters the reactor where it exchanges heat with the SCAM reactant for energy storage. Based on previous work on the reactor's heat storage process^[7], the heliostat field area was determined from known receiver inlet and outlet parameters. The specific operating parameters and thermodynamic equations for the SPT are shown in Tables 9 and 10.

Table 9- Operating parameters of the heliostats and the receiver^[20, 29].

Parameter	Value
DNI	850 W/m ²
$N_{heliostat}$	914
Aheliostat	50 m^2
η_{field}	0.82
$lpha_{rec}$	0.95
em_{rec}	0.85
$A_{receiver}$	300 m^2
$H_{receiver}$	80 m
T_{sun}	5773 K

Inlet temperature of the SPT 800 K Outlet temperature of the SPT 1000 K

Table 10- Thermodynamic equations of the SPT^[29, 30].

Description	Equation
	$\mathcal{G}_{use,rec}^{\mathcal{K}} = n_{HTF}^{\mathcal{K}} \left(h_{rec,e} - h_{rec,i} \right)$
Heat transfer of the receiver	$\mathcal{G}_{use,rec}^{\mathbf{x}} = \alpha_{rec} \cdot \mathcal{G}_{i,rec}^{\mathbf{x}} - \mathcal{G}_{loss,rec}^{\mathbf{x}}$
	$oldsymbol{\mathscr{G}}_{i,rec}^{\!$
	$\mathcal{G}_{loss,rec}^{\mathbf{x}} = \mathcal{G}_{loss,rad}^{\mathbf{x}} + \mathcal{G}_{loss,com}^{\mathbf{x}}$
	$\mathcal{E}_{loss,rad} = A_{rec} \cdot em_{rec} \cdot \sigma \cdot T_{rec}^4$
Radiant heat loss	$\mathcal{E}_{loss,conv} = A_{rec} \cdot \xi_{conv} \cdot (T_{sur,rec} - T_0)$
Convective heat loss	$T_{sur,rec} = T_{rec,e} + 20$
	$\xi_{conv} = 0.577 \times 10^{-6} \left(\frac{T_{sur,rec} - T_0}{H_{tower}} \right)^{0.25}$

305 **2.3.2 Reactor**

311

Energy storage and release processes occur in the packed bed reactor. The reaction is as follows:

$$CaCO3 = CaO + CO2$$

$$\Delta H = 177.9 \text{ kJ/mol}$$
(24)

The reactor dimensions have been detailed in Section 2.2, which includes a total of 200 reactors.

2.3.3 Compressor and turbine

REFPROP 9.1 software provides thermodynamic parameters, and the main component parameters are shown in Table 11. The centrifugal compressor is used, and the compressor outlet temperature and pressure are shown as follow^[31]:

315
$$T_{c,out} = T_{c,in} \left[1 + \left(\pi_c^{(\kappa-1)/\kappa} - 1 \right) / \eta_c \right]$$
 (25)

$$P_{c,out} = \pi_c P_{c,in} \tag{26}$$

where π_c , η_c and κ represent the compression ratio, isentropic efficiency, and adiabatic

318 index respectively.

The turbine outlet temperature and pressure are shown as follows^[32, 33]:

320
$$T_{t,out} = T_{t,in} \left[1 - (1 - \pi_t^{(1-\kappa)/\kappa}) \eta_t \right]$$
 (27)

$$P_{t,out} = P_{t,in} / \pi_t \tag{28}$$

where π_t and η_t represent the expansion ratio and isentropic efficiency, respectively.

Table 11- Main parameters of the components.

Component	Value
Compressor	_
Compression ratio	7.0
Specific heat ratio	1.4
Isentropic efficiency	85 %
Turbine	
Expansion ratio	7.0
Isentropic efficiency	85 %

2.4 Performance indicators

2.4.1 Reactor

324

325

331

332

333

337

To evaluate the exothermic process in the reactor, this study employs three indicators.

The first one is the total reaction time t (s), and Table 12 summarizes the reaction times for all conditions. The second one is the heat release power (HRP in kW) during the exothermic process:

$$HRP = \int Q_{h} dV$$
 (29)

HRP is related to the heat release rate, and it represents the amount of heat released per unit time during the reaction process. The third one is the heat exchange power (HEP in kW) during the exothermic process:

HEP =
$$(\rho c_p)_{HTF} u_{HTF} (T_{out} - T_{in}) A$$
 (30)

HEP represents the heat transferred per unit time by HTF during the heat exchange process, and it provides energy for subsequent expansion work.

Table 12- The summary of exothermic reaction times under different conditions.

NO	Cases	Conditions	Exothermic reaction time (s)
1	Baseline case		8680
2		550 K	12200
3	Temperature	650 K	7520
4		750 K	10800

5		0.3	13000
6	Reactant porosity	0.4	11800
7		0.5	10300
8	CO ₂ inlet volumetric flow	5 L/min	10400
9	rate	15 L/min	7500
10	Addition of intermediate air pathway		6200
11		5 W/m/K	8000
12	Reactant thermal conductivity	10 W/m/K	7010
13		20 W/m/K	6600

2.4.2 Total system

- The energy and exergy efficiencies of the TSTPG system, η_{energy} and η_{exergy} are shown
- 340 as follows:

$$\eta_{energy} = \frac{W_T}{Q_{SPT} + W_C} \tag{31}$$

- 342 where W_T is the net output of electrical power, Q_{SPT} is the heat input from SPT, and W_C
- is the compressor work input.

$$\eta_{exergy} = \frac{Ex_T}{Ex_{SPT,f} + Ex_C} \tag{32}$$

- where Ex_T is the exergy output of the system, $Ex_{SPT,f}$ is the fuel exergy, and Ex_C is the
- exergy input from the compression process.
- Net Present Value (NPV) is used as a key indicator to evaluate the economic viability of
- the TSTPG system. It can help to measure the system's investment returns and economic
- 349 feasibility, thus providing a basis for decision-making^[34]. The calculation of NPV is as
- 350 follows:

$$NPV = \sum_{t=0}^{n} \frac{ATP_t}{(1+i)^t} - C_{investment}$$
 (33)

- where i is the discount rate (i.e., 6%), and t is the lifetime cycle (i.e., 25 years). The total
- investment cost ($C_{investment}$) is shown in Table 13.
- Table 13- Capital cost for component.

SPT
$$Z_{heliostat} = 150 A_{heliostat} N_{heliostat}$$

$$Z_{Receiver} = 1835.7 h_{tower} - 2568 h_{tower} + 3 \times 10^7$$

$$\log C_P = K_1 + K_2 \log V + K_3 \left(\log V\right)^2$$

Reactor
$$k_1 = 4.7116, k_2 = 0.4479, k_3 = 0.0004$$

Compressor
$$\frac{44.71n\%}{0.95 - \eta_c} \left(\frac{P_2}{P_1}\right) \ln\left(\frac{P_2}{P_1}\right)$$

Turbine
$$\left(\frac{301.45n_x^8}{0.94 - \eta_t}\right) \ln \left(\frac{p_3}{p_4}\right) (1 + \exp(0.025T_3 - 1570))$$

HEX
$$\log Z_{Hex}(\$) = k_1 + k_2 \log A_{Hex} + k_3 (\log A_{Hex})^2$$

$$k_1 = 4.3427, \ k_2 = -0.303, \ k_3 = 0.1634$$

Generator 17500 \$

Storage tank
$$\log C_P = K_1 + K_2 \log V + K_3 (\log V)^2$$
$$k_1 = 4.1052, \ k_2 = 0.5320, \ k_3 = -0.0005$$

Annual total profit (ATP) is calculated as follows:

$$ATP = S - C_{O&M} \tag{34}$$

Annual total revenue is shown as follows^[35]:

$$S = c_{elec, peak} \times W_{t} \times y \times t_{dch}$$
 (35)

The annual operating cost is the sum of off-peak electricity prices and maintenance costs of the TSTPG system. Maintenance costs amount to 6% of the annual investment cost:

$$C_{O\&M} = C_{elec} + \phi \times C_{A,imestment}$$
 (36)

$$C_{elec} = c_{elec,off-peak} \times W_c \times y \times t_{ch}$$
 (37)

- 363 where $c_{elec,peak}$ and $c_{elec,off-peak}$ represent the high and low valley electricity prices,
- respectively; ϕ and y denote the system maintenance factor and annual operation time,
- 365 respectively.
- The capital recovery factor (CRF), which is influenced by the discount rate and equipment lifespan, is given below:

$$CRF = \frac{i(1+i)^n}{(1+i)^n - 1}$$
 (38)

$$C_{A investment} = CRF \times C_{investment} \tag{39}$$

In addition, the total annual cost (TAC) includes $C_{A,investment}$ and $C_{O\&M}$:

$$TAC = C_{A.investment} + C_{O\&M}$$
 (40)

The dynamic payback period (DPP) is as follows^[36]:

$$DPP = |DPP - 1| + \frac{|NPV_{|DPP - 1|}|}{ATP_{|DPP|}}$$
 (41)

- where |DPP-1| is the last year in which the NPV is negative.
- In contrast to the fossil fuel power plants, the thermochemical solar thermal system can be operated without consuming the fossil fuels, instead of deriving energy exclusively from the solar power and calcium-based materials. It can naturally eliminate the fuel consumption and carbon dioxide emissions^[37, 38].

$$M_{\text{Petro}} = \alpha_{\text{Petro}} \times N \times W_T \tag{42}$$

$$M_{\text{CO}_2} = \alpha_{\text{CO}_2} \times N \times W_T \tag{43}$$

- where α_{Petro} represents the average crude oil (0.266) and α_{CO_2} represents the carbon dioxide emissions from fossil fuels (0.849). During system operation, no CO₂ is produced, resulting in zero emissions.
 - 3. Results of the exothermic process in the packed bed reactor

3.1 The baseline case

384

385

386

387

388

389

390

391

392

The exothermic process in an indirect cylindrical packed bed reactor using air and CO₂ was studied, with a total reaction time of 8680s. As shown in Fig. 6(a), as the exothermic process progresses, due to the indirect heat exchange method, the reaction zone permeates diagonally upward from the exterior to the interior, aligning with the flow directions of CO₂ and air and resulting in a "V" shape. Consequently, as shown in Fig. 6(b), the heat storage reaction at points D, E and F on the outer wall rapidly increases to 0.85. Interestingly, points A, B and C on the inner wall exhibit a period of stable reaction. This occurs because points

A, B and C generate higher temperatures and cannot exchange heat with HTF in a timely manner. According to Eq. (7), the equilibrium equation limits the reaction rate, resulting in a stable period in reaction progress. As HTF promptly transfers heat from points A, B and C, the exothermic reaction at these points rapidly resumes.

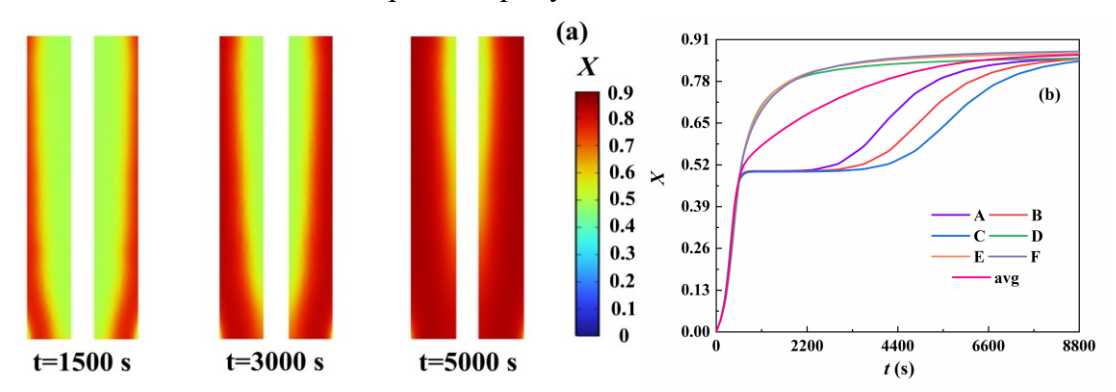


Fig. 6 Baseline case results: (a) Reaction extent contours and (b) Reaction extent variations at monitoring points.

As shown in Fig. 7(a), the temperature in the external reaction zone first decreases because the exothermic reaction ends and the reactants are cooled by low-temperature HTF at the reactor outer wall. When CO_2 flows through the reactants, intense exothermic reactions occur, raising the temperature to reach an equilibrium state. As the exothermic process continues, the local temperature in the unreacted zone also rises to an equilibrium temperature. Based on Eq. (7), the reaction rate decreases, resulting in a local cessation of the exothermic reaction. This aligns with the results shown in Fig. 6. As shown in Fig. 7(b), the monitoring points A, B, C, D, E and F all experience rapid temperature increases due to the exothermic reaction. The cooling effect of low-temperature HTF at the reactor outer wall makes temperature decrease at points D, E and F. Due to the sequential flow of low-temperature HTF through points D, E and F, the maximum temperatures follow the order F > E > D. As the inner points A, B and C cannot exchange heat with HTF promptly, they exhibit a period of stable peak temperature, which explains the stable period in reaction progress at points A, B and C shown in Fig. 6(b). As low-temperature HTF takes heat away, the temperatures at points A, B and C decrease, following a similar sequential pattern at points D, E and F.

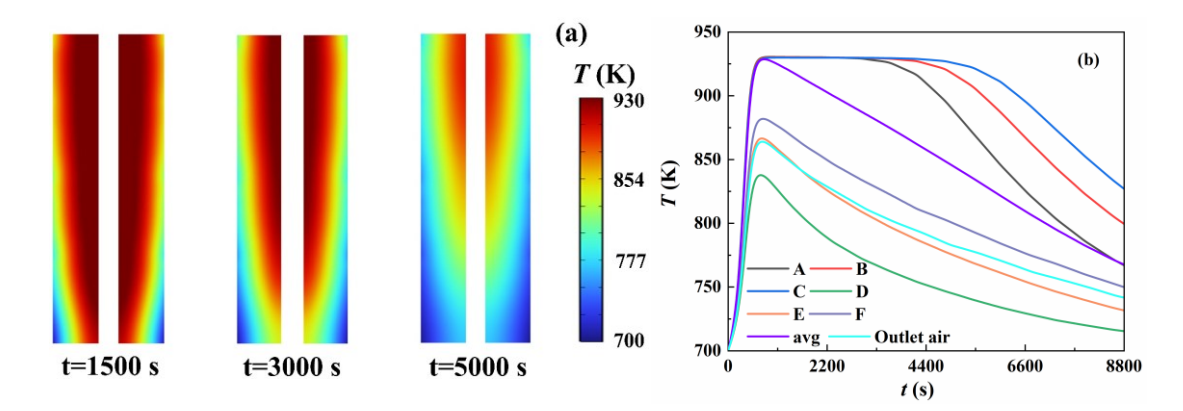


Fig. 7 Temperature evolution in baseline case: (a) Temperature distribution contours and (b) Temperature variations at monitoring points.

As shown in Fig. 8(a), a "V" shape appears inside the reactor and moves along the axial axis, similar to the patterns shown in Figs. 6 and 7. As shown in Fig. 8(b), due to intense local exothermic reactions, the monitoring points show steep reaction rate slopes. The reaction rate peaks at points A, B and C are lower than those at points D, E and F due to cooling by low-temperature HTF. As the exothermic reaction progresses, points A, B and C show a second peak in reaction rate, as the local heat is transferred to low-temperature HTF, allowing the exothermic reaction to resume. Although Eq. (6) indicates that higher temperatures lead to faster reaction rates, the equilibrium equation restricts the reaction rate at high temperatures, creating a mutual constraint. The following discussions focus on the effect of initial temperature on the exothermic process.

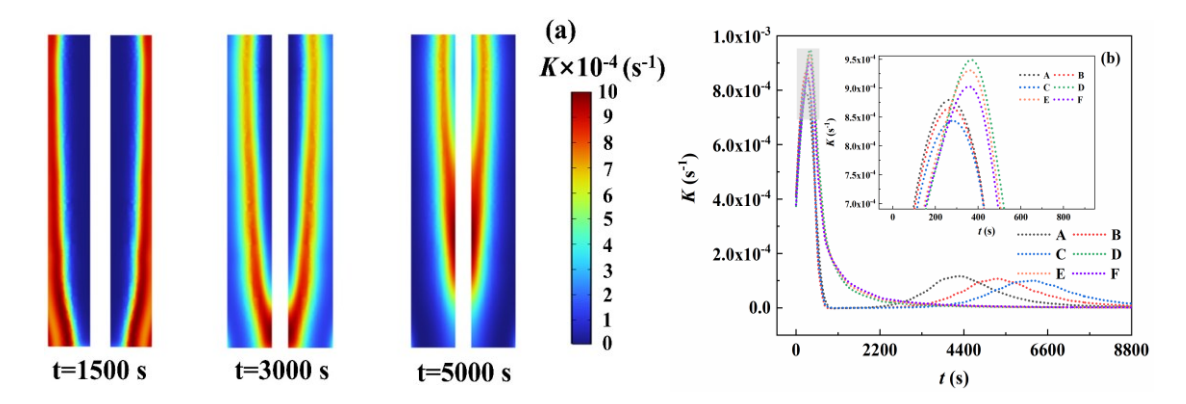


Fig. 8 Reaction rate in baseline case: (a) Reaction rate distribution contours and (b) Reaction rate variations at monitoring points.

Fig. 9(a) shows the pressure changes at monitoring points. During the exothermic process, CO₂ is strongly consumed by local reactions, causing rapid pressure drops in the

reactor. Subsequently, CO₂ diffuses uniformly throughout the system and generates significant reaction heat, leading to sharp pressure increases at the monitoring points. Interestingly, monitoring points at the same horizontal level show highly consistent pressure changes, indicating that CO₂ content does not affect reaction progress at these points. Pressure data shows smaller variations at the CO₂ inlet and larger variations at the outlet. This is due to increased CO₂ diffusion resistance from low reactant porosity. Additionally, at the CO₂ inlet where consumption occurs, continuous supply of large amounts of CO₂ leads to thermal expansion.

The overall performance of the exothermic reaction is shown in Fig. 9(b). The exothermic reaction maintains intense heat release within 900s, with a peak heat release power of 25 kW and high thermal utilization efficiency during this period. Subsequently, the exothermic process reaches a steady state. The heat exchange power peak appears around 1800s, showing a delay relative to the initial exothermic reaction due to indirect heat exchange. When the reaction power falls below a specific threshold, the reactor cannot meet the industrial heating requirements^[39].

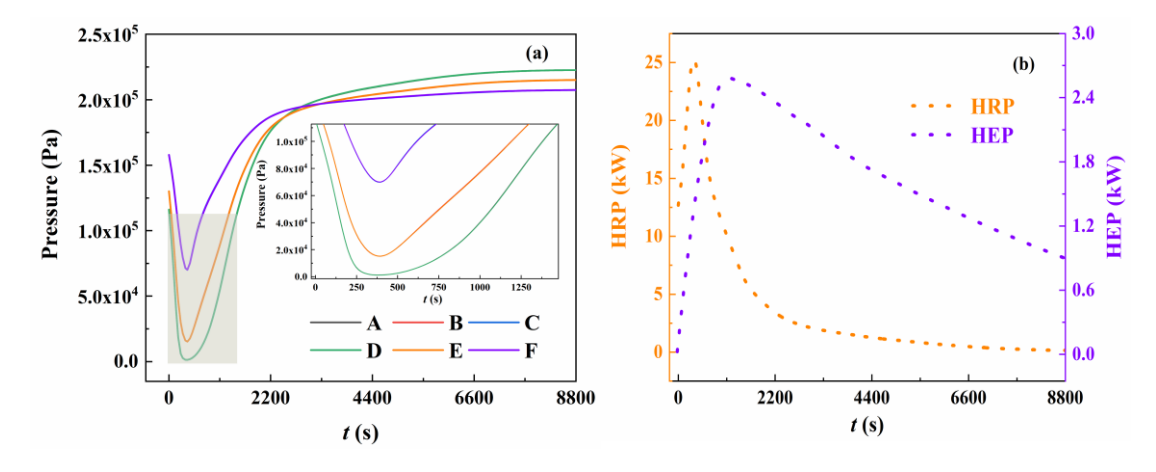


Fig. 9 (a) The pressure variation of the baseline case and (b) Overall performance of the baseline case.

3.2 The impact of temperature

In previous research, Tian et al.^[17] found that temperatures between 550-750°C had minimal impact on exothermic performance, while temperatures below 450°C showed significant effects. According to Eqs. (6), (7) and (30), both initial temperature and inlet temperature affect the reaction rate and heat exchange processes. In this section, initial and

inlet temperatures are set at 550 K, 650 K, and 750 K along with other conditions identical to the baseline case. As shown in Table 12, the shortest exothermic time occurs at 650 K.

As shown in Fig. 10(a), reaction progress rapidly increases at temperatures of 650 K, 700 K and 750 K and then slows due to reaction equilibrium constraints. At temperatures above 650 K, closer proximity to equilibrium temperature extends the exothermic time. At 550 K, initial reaction progress is slow. However, as large amounts of heat are released during the exothermic process, the reaction rate increases, leading to a final reaction progress which only reaches 0.76. As shown in Fig. 10(b), both HRP and HEP reach their maximum values at 650 K. When selecting appropriate temperatures, it needs to balance the relationship between the Arrhenius equation and equilibrium equation, ensuring ideal reaction rates to maintain good reaction equilibrium.

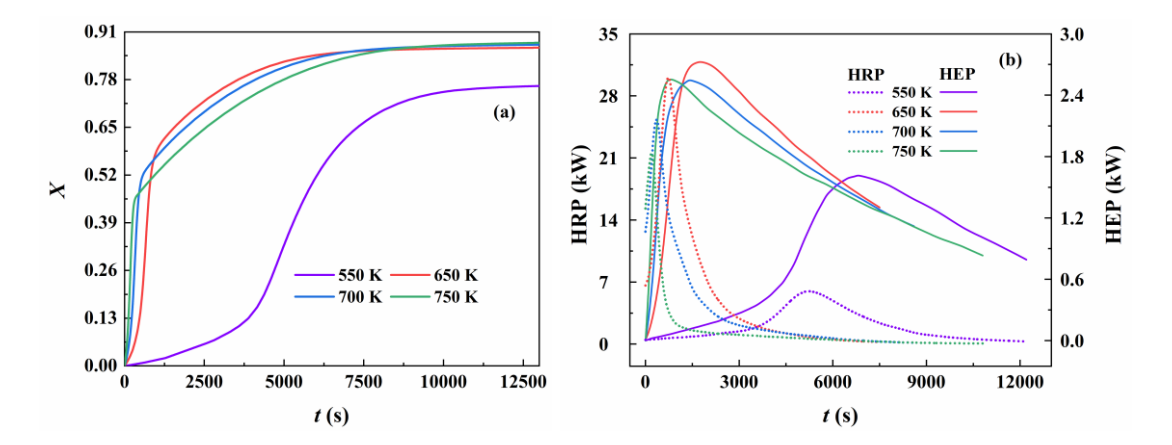


Fig. 10 The impact of temperature on the exothermic process: (a) The variation in reaction extent and (b) Overall performance variation with different temperatures.

3.3 The impact of the reactant porosity

In the above discussions, reactant porosity was kept constant at 0.6. This section examines the impact of porosity on the exothermic process. As shown in Fig. 11(a), decreasing porosity significantly increases the reaction time. This is due to increased reactant concentration and decreased permeability, which increases the flow resistance for CO₂ passing through the reactor. As shown in Fig. 11(b), evaluation of exothermic capacity under different porosities reveals that lower porosity significantly extends the duration of maximum HRP and HEP in the reactor, demonstrating a notable heat release performance.

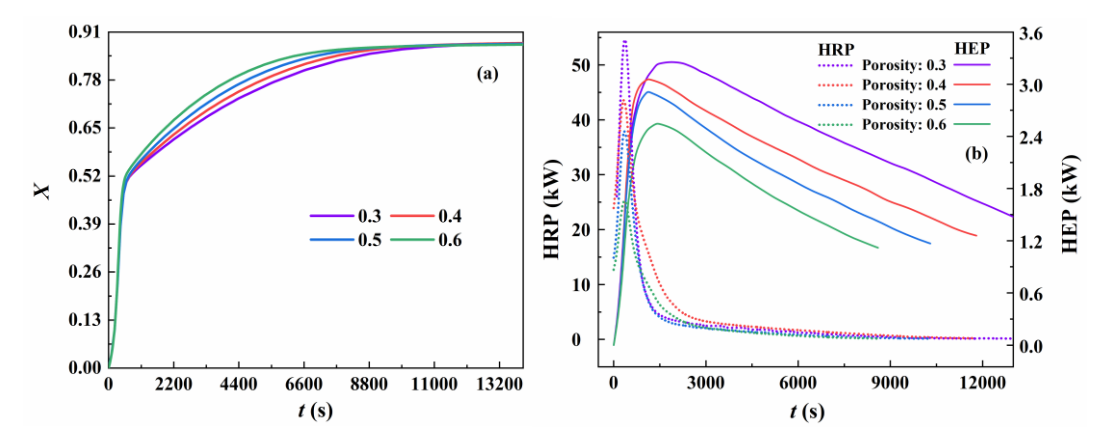


Fig. 11 The impact of reactant porosity on the exothermic process: (a) The variation in reaction extent and (b) Overall performance variation with different reactant porosities.

3.4 The impact of CO₂ inlet volumetric flow rate

In this section, CO₂ inlet volumetric flow rates of 5 L/min and 15 L/min are studied, and all other conditions are kept constant as in the baseline case. As shown in Fig. 12(a), increasing the CO₂ inlet volumetric flow rate significantly shortens the reaction time. This can be attributed to two factors: first, higher inlet flow rate increases the CO₂ supply rate, thereby accelerating the reaction with the reactants; second, larger mass flow rate facilitates the faster heat removal during the exothermic process, effectively reducing temperature buildup within the system. As a result, the reaction rate is enhanced due to the lowered equilibrium temperature. As shown in Fig. 12(b), both HRP and HEP increase as the volumetric flow rate increases.

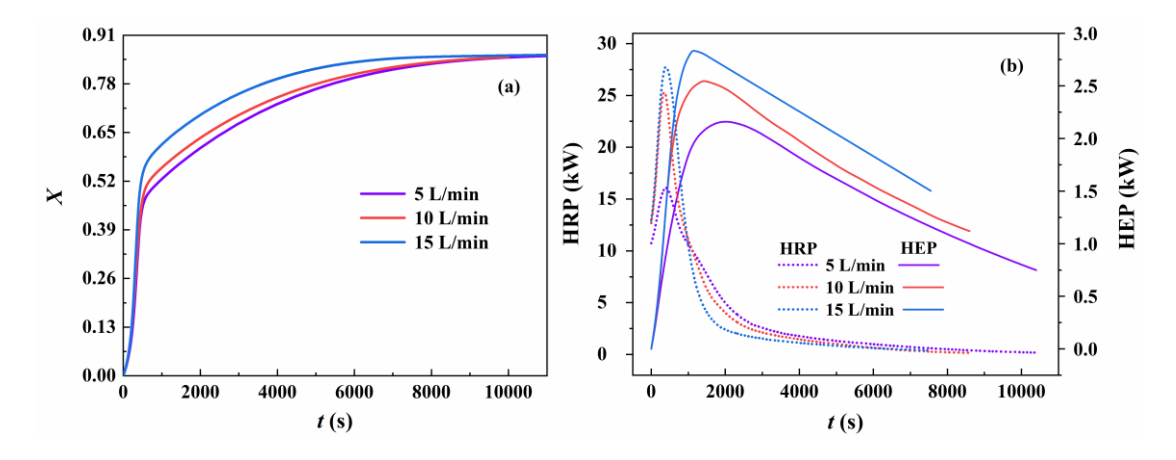


Fig. 12 The impact of CO₂ inlet volumetric flow rate on the exothermic process: (a) The variation in reaction extent and (b) Overall performance variation with different CO₂ inlet volumetric flow rates.

3.5 The impact of the addition of an intermediate air pathway

Based on the above study, it is obvious that increasing the low-temperature HTF flow rate to remove heat during the exothermic process in the reactor is of significant importance. We have added HTF channels to lower the temperature within the reactor. As shown in Fig. 13(a), the concentration distribution curves in the reactor with additional HTF channels differ significantly from the baseline case. The reaction progress inside the reactor is more uniform, especially in the early stages (e.g., t=1500 s), where the concentration gradient within the reactor is notably reduced. This indicates that the added HTF channels effectively can help improve the heat distribution and reduce the local overheating, thereby enhancing the overall reaction efficiency and uniformity. Furthermore, in the later stages (t=5000 s), the reaction is essentially complete, demonstrating that adding channels can significantly accelerate the reaction progress. Fig. 13(b) shows the temperature cloud diagrams in the reactor over time. In the initial stage (t=1500 s), the low-temperature zone is mainly concentrated in the lower part of the reactor, showing distinct temperature gradients. it also indicates that lowtemperature HTF effectively removes heat. In the middle stage (t=3000 s), the lowtemperature zone gradually expands upward, and temperature gradients significantly decrease, showing that the added HTF channels can effectively enhance the heat transfer efficiency. In the later stage (t=5000 s), the temperature distribution inside the reactor tends to become uniform. As shown in Fig. 13(c), the exothermic time with added air channels is 6200 s, which is reduced by 2480 s. As shown in Fig. 13(d), with added air channels, HRP rapidly rises to 27.23 kW in the initial reaction stage and decreases slowly, indicating that the addition of channels makes the heat release process more stable. Meanwhile, HEP significantly increases with added channels, effectively enhancing the heat transfer. This design optimizes the heat transfer by effectively reducing the local overheating risks and improves the stability and thermal energy utilization of the exothermic process.

496

497

498

499

500

501

502

503

504

505

506

507

508

509

510

511

512

513

514

515

516

517

518

519

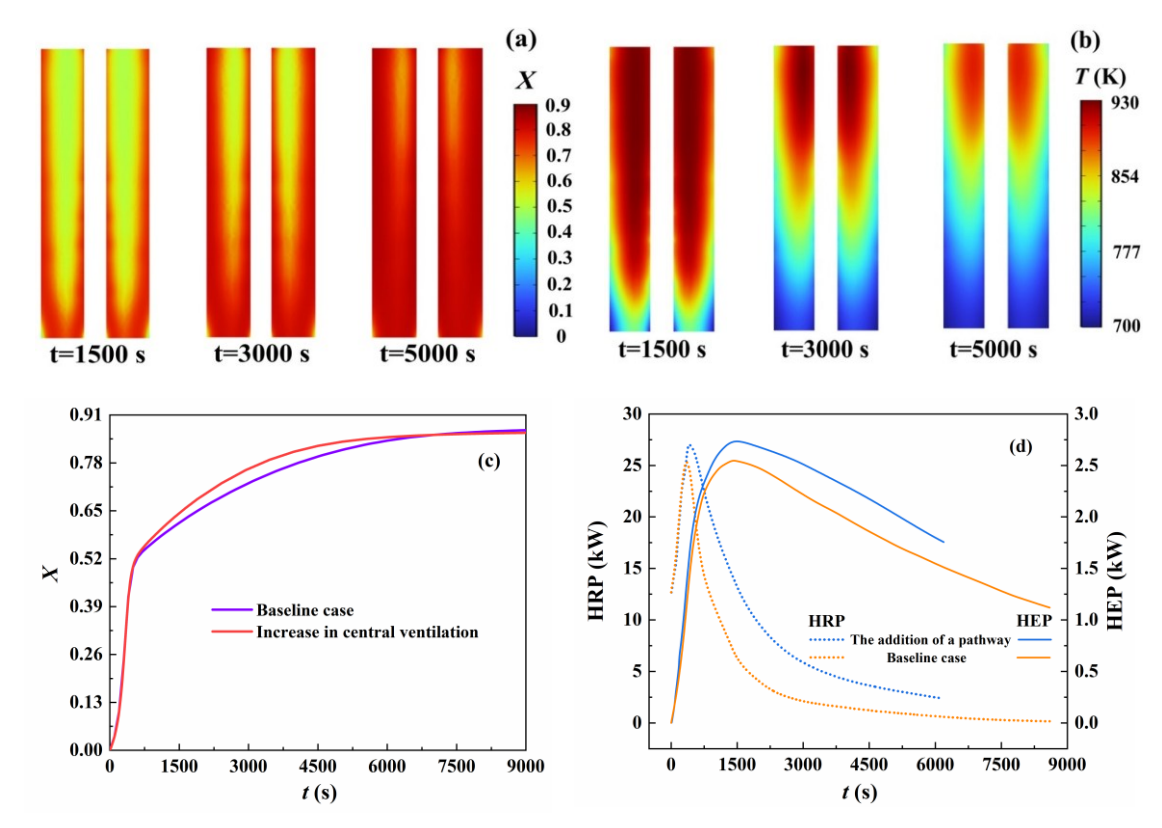


Fig. 13 Effect of intermediate air pathway: (a) Reaction extent contours; (b) Temperature distribution contours; (c) Reaction extent variation; and (d) System performance.

3.6 The impact of the reactant thermal conductivity

A variety of researchers^[2, 40] have enhanced the thermal conductivity of calcium-based materials through doping to enhance their effective reaction rates. Therefore, it is meaningful to analyze the performance of calcium-based materials with varying thermal conductivity coefficients in packed bed reactors^[17]. As shown in Fig. 14(a), enhancing the thermal conductivity of the reactants can significantly shorten the exothermic reaction time. This is because a higher thermal conductivity allows the heat released during the reaction to transfer more rapidly from the reaction zone to the outer wall, where the low-temperature HTF is located, thereby reducing the thermal non-uniformity and limiting the phenomenon of local heat accumulation. As shown in Fig. 14(b), increasing the reactant thermal conductivity significantly increases both HRP and HEP. HRP peaks are higher and reached earlier, indicating that higher thermal conductivity can accelerate reaction rates and heat release. The overall trend of HEP is similar to HRP but shows a slight time lag due to the time required for heat transfer from the reaction zone to HTF. By optimizing the thermal conductivity of filling materials (such as adding high thermal conductivity materials), the reaction process

can be accelerated and heat transfer efficiency is improved, showcasing an important strategy for enhancing system performance.

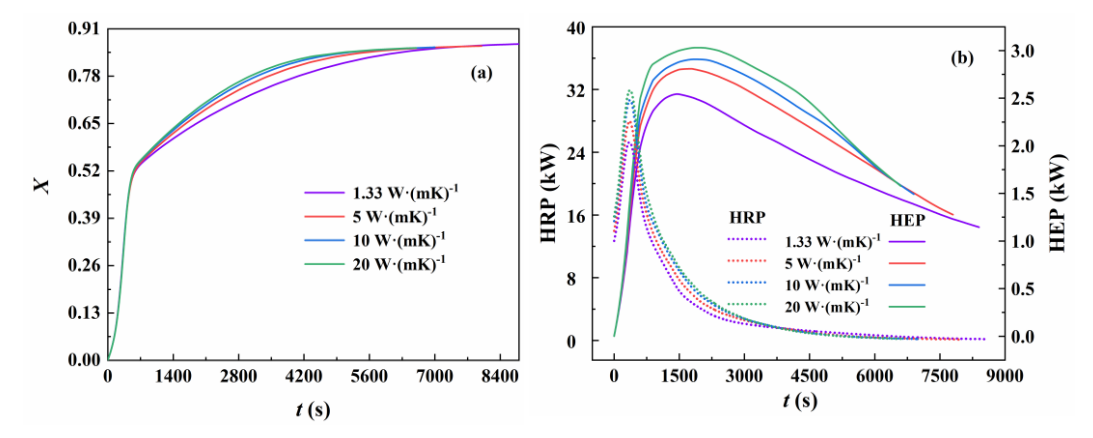


Fig. 14 The impact of the reactant thermal conductivity on the exothermic process: (a) The variation in reaction extent and (b) Overall performance variation with different reactant thermal conductivities.

4. Results of thermochemical solar thermal power generation system

4.1 Energy, exergy, economic and environmental analysis

539

540

541542

543

544

545

546

547

548

549

550

551

552

553

554

555

556

557

558

559

560

561

562

Since the reactor plays a crucial role in thermal energy utilization in TSTPG system, this study for the first time systematically investigates its impact on the proposed system from the reactor perspective. To this end, this study employs a 4E analysis framework (energy, exergy, economy, and environment) to comprehensively evaluate the system performance, focusing on the analysis for the mechanism of reactor parameter optimization to improve the system energy efficiency, reduce the exergy loss, decrease CO₂ emissions and optimize economic benefits. The thermodynamic properties at various cycle points are shown in Table 14. Table 15 displays the power generation of the TSTPG system under different conditions. Fig. 15(a) presents the energy streamline of the TSTPG system based on the packed bed reactor in baseline case. The system receives input energy (73.62 MWh) and compression work (31.11 MWh) from SPT. The total stored energy is 91.37 MWh with 20.38 MWh storage loss during the heat storage process. Through the exothermic reaction in the packed bed reactor, an amount of 70.99 MWh energy is released with 14.78 MWh release loss. The system finally outputs 56.21 MWh of electrical work. Furthermore, as depicted in Fig. 15(b), the fuel exergy $(Ex_{SPT,f})$ significantly exceeds the heat of the SPT (Q_{SPT}) , resulting in an exergy efficiency that is lower than the energy efficiency.

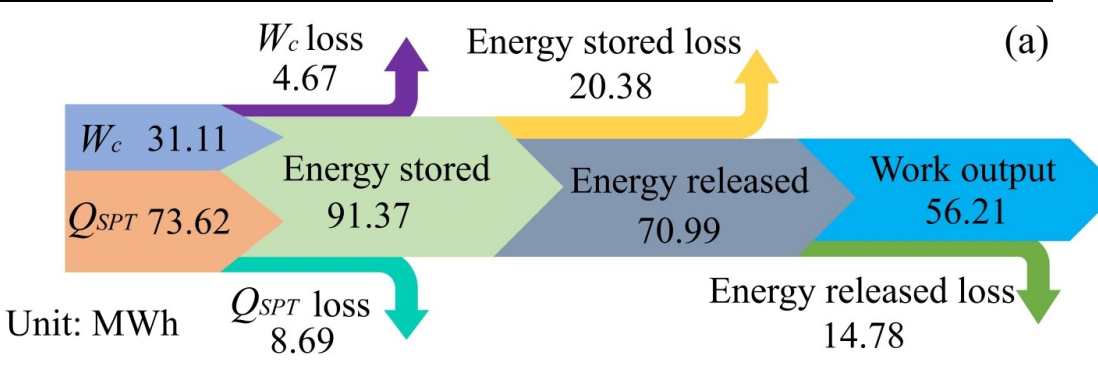
Table 14- Thermodynamic characteristics at different points.

	1	2	3	4	5	6	7	8	9
Temperature (K)	1000	1000	700	308	578	566	325	700	1000
Pressure (bar)	7	1	1	1	7	7	1	1	7
\dot{E}_{χ} (MW)	60.58	1.38×10^{-2}	5.5×10 ⁻³	0	6×10^{-3}	6×10^{-3}	0	1.47×10^{-3}	60.58
Mass flow rate (kg/s)	112.28	3.5×10 ⁻²	3.5×10 ⁻²	3.5×10 ⁻²	3.5×10 ⁻²	3.5×10^{-2}	3.5×10^{-2}	6.2×10^{-2}	112.28
	10	11	12	13	14	15	16	17	18
Temperature (K)	1000	700	750	430	430	806	1000	700	700
Pressure (bar)	7	7	7	1	1	7	1	1	1
\dot{E}_{x} (MW)	60.58	36.55	45.48	0.75	0.75	45.48	1.15×10 ⁻¹	4.95×10 ⁻²	4.95×10 ⁻²
Mass flow rate (kg/s)	112.28	112.28	112.28	112.28	112.28	112.28	0	0	0

Table 15- Electricity generation of thermochemical solar thermal power systems under

565 different conditions.

NO	Cases	Conditions	Electricity generation (MWh)
1	Baseline case		56.21
2		550 K	76.47
3	Temperature	650 K	48.31
4		750 K	70.37
5		0.3	84.39
6	Reactant porosity	0.4	76.52
7		0.5	66.73
8	CO ₂ inlet volumetric flow	1000 L/min	67.06
9	rate	3000 L/min	48.43
10	Addition of intermediate air pathway		40.32
11		5 W/m/K	51.93
12	Reactant thermal conductivity	10 W/m/K	45.49
13		20 W/m/K	43.01



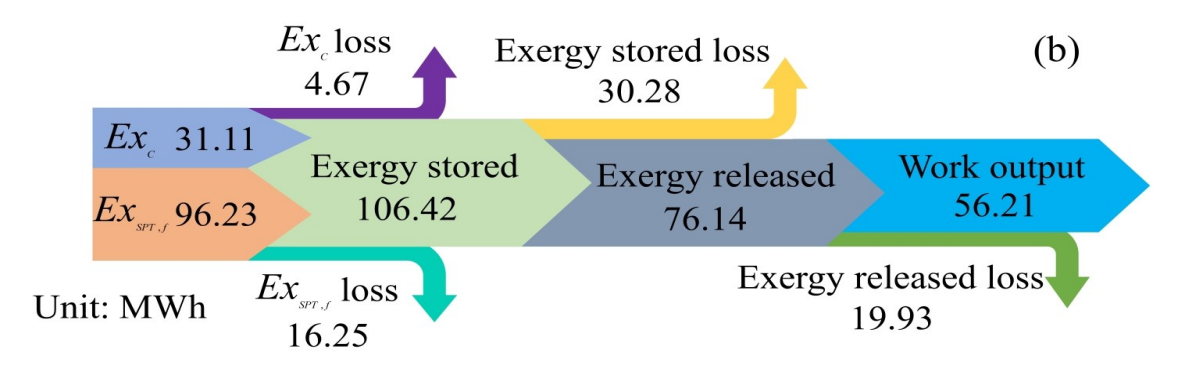


Fig. 15 The streamline of TSTPG system: (a) Energy and (b) Exergy.

567

568

569

570

571

572

573

574

575

576

577

578

579

580

581

582

583

584

585

586

587

588

589

590

591

As shown in Fig. 16(a), as the temperature increases from 550 K to 750 K, the system's energy and exergy efficiencies increase first before decreasing, reaching peak values of 56.85% and 49.06% respectively at 650 K. This is mainly because this temperature point achieves the optimal compromise between the reaction kinetics and thermodynamic equilibrium, resulting in the highest exothermic efficiency in the reactor. Meanwhile, CO₂ emission reduction and fossil fuel reduction show similar trends, but the system's TAC increases with temperature, indicating that higher operating temperatures bring greater economic burden. By considering all indicators comprehensively, 650 K is identified as the optimal operating temperature for the system. As shown in Fig. 16(b), as the reactant porosity increases from 0.3 to 0.6, the system's energy and exergy efficiencies show a clear downward trend, decreasing from 58.31% to 53.67% and from 50.04% to 44.14%, respectively. Similarly, CO₂ emission reduction and fossil fuel reduction also show declining trends, while the system's annual TAC slightly decreases with the increasing of porosity. This can be explained as follows. Although lower porosity increases the reactant concentration and reaction time, it also improves the reactor's heat storage and utilization efficiency. As a result, better overall performance is observed. As shown in Fig. 16(c), changes in CO₂ volumetric flow rate significantly affect the system's comprehensive performance. As the flow rate increases from 1000 L/min to 3000 L/min, the system's energy and exergy efficiencies show notable nonlinear characteristics, reaching 53.67% and 44.14% respectively at 2000 L/min. In contrast, CO₂ emission reduction and fossil fuel replacement rates keep declining with the increasing of flow rate. It is mainly because higher flow rates reduce the reactor exothermic time, leading to a decreased power generation. Meanwhile, the system's TAC reaches the minimum value at a CO2 flow rate of 2000 L/min before beginning to increase, indicating the presence of an optimal CO₂ flow rate

range where both technical and economic performance are most effectively balanced. As shown in Fig. 16(d), adding intermediate air channels significantly improves the reactor exothermic efficiency. Compared to the baseline case, adding intermediate air channels increases the system's energy and exergy efficiencies from 53.67% to 54.96% and from 44.14% to 45.61%, respectively. This improvement is mainly attributed to enhanced convective heat transfer which reduces the local temperature accumulation. However, CO2 emission reduction and fossil fuel replacement rates show opposite trends, indicating that although air channel improvements enhance the reactor exothermic efficiency, they somewhat affect the system power generation. Notably, the system's TAC also slightly increases with air channel optimization, reflecting the trade-off between the heat transfer performance improvement and economic costs. As shown in Fig. 16(e), enhanced reactant thermal conductivity significantly improves the system performance. As the thermal conductivity is enhanced from 1.33 W/(m·K) to 20 W/(m·K), the system's energy and exergy efficiencies show a continuous upward trend, which is mainly attributed to promote the heat transfer within the reactor. However, CO₂ emission reduction and fossil fuel replacement rates show continuous declining trends, indicating that although increased thermal conductivity improves the exothermic efficiency, it somewhat reduces the system power generation. Meanwhile, the system's TAC decreases with the increasing of thermal conductivity, indicating that improving material thermal conductivity can achieve economic optimization while maintaining the system performance.

592

593

594

595

596

597

598

599

600

601

602

603

604

605

606

607

608

609

610

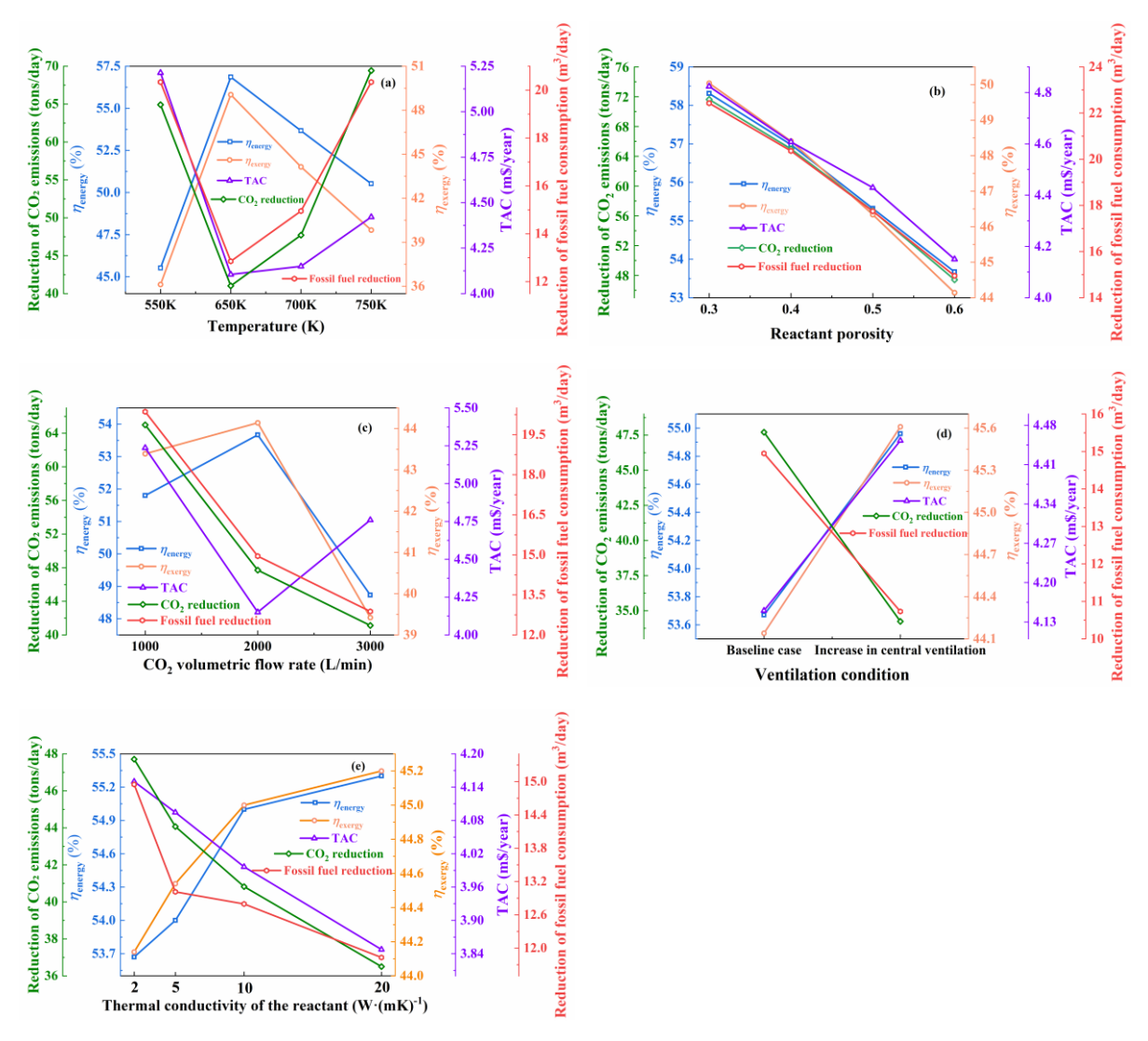


Fig. 16 4E analysis of the exothermic process in the reactor for thermochemical solar power systems: (a) Temperature effect; (b) Porosity effect; (c) CO₂ flow rate effect; (d) Ventilation effect; and (e) Thermal conductivity effect.

Based on the economic model established in Section 2, this study conducted an economic assessment of the TSTPG system. System operational data shows: during off-peak electricity demand periods (0.046 \$/kWh), the system uses solar energy for energy storage; during peak periods (0.264 \$/kWh), electricity is generated through exothermic reactions and sold. As shown in Fig. 17, the payback period for the TSTPG system is 12.53 years.

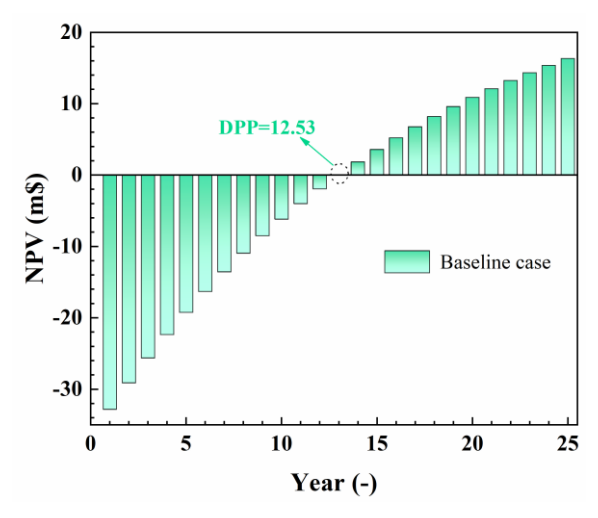


Fig. 17 NPV and DPP of TSTPG system.

621

623

624

625

626

627

628

629

631

632

633

4.2 Comprehensive appraisal via entropy-TOPSIS

To provide an objective and fair evaluation system, this study uses the entropy weight method to quantify the weights of various indicators. The procedure for determining indicator weights based on the entropy weight method is as follows:

Frist, standardize the assessment metrics.

The TSTPG system has 13 operating modes and 5 evaluation indicators, so the indicator matrix is:

630
$$\mathbf{A} = \begin{bmatrix} b_{11} & b_{12} & \mathbf{L} & b_{1m} \\ b_{21} & b_{22} & \mathbf{L} & b_{2m} \\ \dots & \dots & \dots \\ b_{n1} & b_{n2} & \dots & b_{nm} \end{bmatrix}$$
(44)

The evaluation indicators are divided into positive and negative types, with data normalization as follows:

Positive indicators:

$$a_{ij} = (b_{ij} - minb_j) / (maxb_j - minb_j)$$
(45)

Negative indicators:

$$a_{ij} = \left(maxb_j - b_{ij}\right) / \left(maxb_j - minb_j\right)$$
(46)

where b_{ij} represents the value at position j in working mode i, max b_j and min b_j are the maximum and minimum values of index j, respectively, and $A' = [a_{ij}]_{n \times m}$ is the normalized indicator matrix.

Second, determine the normalized specific gravity values for each element a_{ij} .

$$P_{ij} = \frac{a_{ij}}{\sqrt{\sum_{i=1}^{n} a_{ij}^2}}$$
 (47)

$$E_{j} = -\frac{1}{\ln n} \sum_{i=1}^{n} P_{ij} \ln P_{ij}$$
 (48)

- where p_{ij} represents the weight of each indicator in total value. If $p_{ij} = 0$, then $P_{ij} ln P_{ij} = 0$,
- and *n* denotes the number of evaluation indicators.
- Third, the entropy weights of each indicator are as follows:

646
$$\omega_{j} = \frac{1 - E_{j}}{\sum_{j=1}^{m} (1 - E_{j})}, (j = 1, L, m)$$
 (49)

- The smaller value of ω_j , the less useful information the evaluation indicator conveys,
- 648 indicating a reduced contribution to the overall evaluation.
- TOPSIS is a decision-making method, which can be used to evaluate and rank multiple
- alternatives. It scores each alternative by calculating the distances to both the ideal and worst-
- case scenarios. This method has been applied to rank and analyze the five evaluation
- indicators of the TSTPG system.
- The calculation process is as follows:
- Step 1: Determine the weighted normalized decision matrix:

$$X_{ij} = \omega_j a_{ij} \tag{50}$$

- where ω_j indicates the indicator weight, and a_{ij} refers to the normalized matrix.
- Step 2: Determine the positive ideal solution X^+ and the negative ideal solution X^- :

658
$$X^{+} = \{ \max X_{ij} \}, (j = 1, L, m)$$
 (51)

659
$$X^{-} = \{minX_{ij}\}, (j = 1, L, m)$$
 (52)

Step 3: Calculate the Euclidean distance.

661
$$D_i^+ = \sqrt{\sum_{j=1}^m (X_{ij} - X_J^+)^2}, (i = 1, L, n)$$
 (53)

662
$$D_{i}^{-} = \sqrt{\sum_{j=1}^{m} (X_{ij} - X_{J}^{-})^{2}}, (i = 1, L, n)$$
 (54)

where D_i^+ and D_i^- represent the Euclidean distances between the *i*-th evaluation unit, and the positive ideal solution X_J^+ , and the negative ideal solution X_J^- , respectively. The magnitudes of these distances indicate how closely the evaluation object approaches to the ideal solutions.

Step 4: Calculate the relative closeness.

$$Q_{i} = \frac{D_{i}^{-}}{D_{i}^{-} + D_{i}^{+}}$$
 (55)

The closer value of Q_i to 1, the more optimal the overall performance of the alternative.

Alternatives are ranked and classified based on the value of Q_i .

To accurately evaluate the system performance under different operating conditions, this study employs indicators per unit time for assessment. In terms of power generation performance, power generation capacity (MW) rather than power generation (MWh) is chosen as the evaluation indicator. This is because power generation is more related to the reactor's exothermic time, and under different conditions (such as changes in temperature, porosity, CO₂ flow rate, etc.), there are significant differences in reaction completion time (see Table 12). These time differences would mask the system's true power generation capability. Similarly, in environmental benefit assessment, CO₂ emission reduction rate (tons/h) rather than total emission reduction (tons) is selected as the evaluation indicator. Although longer reaction times lead to increased cumulative emission reductions, this does not truly reflect the system's emission reduction efficiency. Table 16 shows the original decision matrix for evaluating the performance of the TSTPG system.

Table 16- Original decision matrix for the entropy-TOPSIS comprehensive evaluation.

NO	Generated power (MW)	$\eta_{\it energy}(\%)$	$\eta_{ m exergy}(\%)$	TAC (m\$/year)	Carbon dioxide emission reduction rate (tons/h)
1	23.31	53.67	44.14	4.15	19.79
2	22.56	45.52	36.12	5.21	19.16
3	23.13	56.86	49.06	4.11	19.64

4	23.46	50.52	39.83	4.42	19.91
5	23.37	58.31	50.04	4.82	19.84
6	23.35	56.98	48.41	4.61	19.83
7	23.32	55.32	46.34	4.43	19.80
8	23.21	51.8	43.39	5.24	19.71
9	23.25	48.73	39.42	4.76	19.74
10	23.41	54.96	43.61	4.45	19.88
11	23.37	53.21	43.37	4.09	19.83
12	23.36	55.01	45.04	3.99	19.86
13	23.46	55.3	45.2	3.95	19.91

Fig. 18 displays the entropy (E_j) and weights (ω_j) of various evaluation indicators calculated based on the entropy weight method. The results show that TAC has the highest weight coefficient (31.50%), reflecting that economic cost remains the primary challenge in TSTPG system. This is followed by exergy efficiency (22.39%) and energy efficiency (19.63%), indicating that system energy utilization efficiency is also an important evaluation indicator. Environmental benefits (13.41%) and power generation capacity (13.07%) have relatively lower weights but still significantly impact the comprehensive system evaluation. The information entropy values of all indicators are high (>0.91), indicating reasonable selection of evaluation indicators and uniform data distribution. The weight distribution shows distinct gradient characteristics (13.07%-31.50%), reflecting the multi-level nature of system performance evaluation. The combined weights of TAC and exergy efficiency exceed 50%, emphasizing the dominant position of system economics and energy quality in the evaluation system. This weight distribution pattern reveals the trade-offs among the economic feasibility, energy utilization efficiency and environmental friendliness.

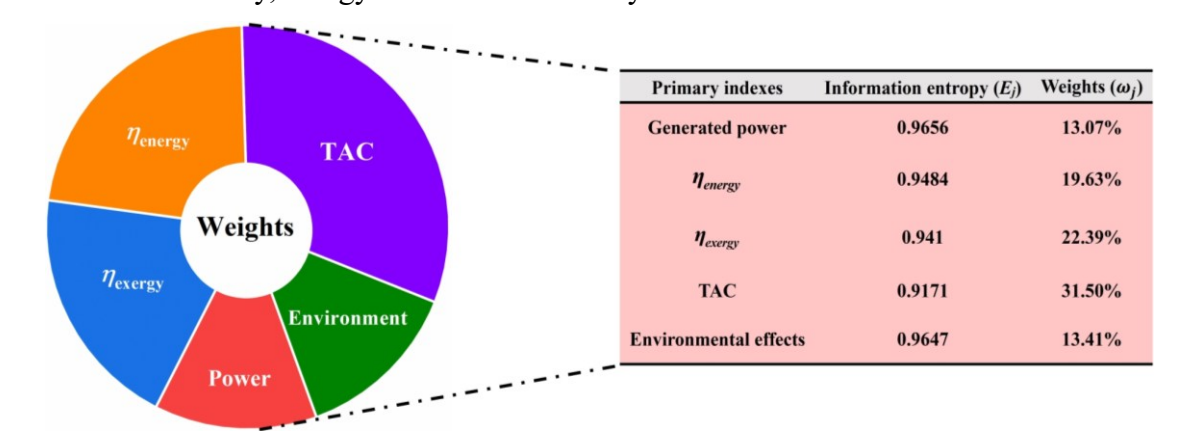


Fig. 18 The weight of evaluation index.

699

700

701

702

703

704

705

706

707

708

709

710

711

712

713

714

715

716

717

718

719

720

721

722

723

724

725

Fig. 19 presents the multi-dimensional evaluation results and comprehensive scores of the TSTPG system under 13 operating conditions based on the entropy-TOPSIS method. The radar chart intuitively displays the performance of each condition across different evaluation dimensions, and larger outer circle values indicate the superior performance. Similar performance is observed under most conditions for power generation capacity (23.21-23.46 MW) and carbon emission reduction rate (19.16-19.91 tons/h), but significant differences are obvious in energy efficiency (45.52%-58.31%), exergy efficiency (36.12%-50.04%) and TAC (3.95-5.24 m\$/year). Comprehensive scoring results show that Case 3 (temperature at 650 K) achieves the highest score (0.8296), mainly due to its higher energy efficiency (56.86%) and exergy efficiency (49.06%) as well as moderate TAC cost. In contrast, Case 8 (CO₂ flow rate of 1000 L/min) receives the lowest comprehensive score (0.3689), which is attributed to its higher TAC and relatively lower energy utilization efficiency. The results indicate that the system performance cannot be justified by a single indicator. Instead, it requires comprehensive consideration of various performance indicators' weights and their interactions. The multi-dimensional evaluation results, which are based on the entropy-TOPSIS method, provide novel guidance for system optimization design and operational parameter selection.

Comparing with existing systems, our TSTPG system demonstrates notable advancements through reactor-level optimization. For instance, Zhang et al. [13] developed a solar-thermochemical energy storage based trigeneration system and achieved energy and exergy efficiencies of 56.92% and 35.94%, respectively. Our system, while focusing solely on power generation, reaches comparable energy efficiency (56.86%) and significantly higher exergy efficiency (49.06%) under optimal conditions (650 K). These improvements can be attributed to our comprehensive investigation of exothermic reaction characteristics and systematic parameter optimization through entropy-TOPSIS evaluation, which provides new insights for the design and operation of thermochemical energy storage systems.

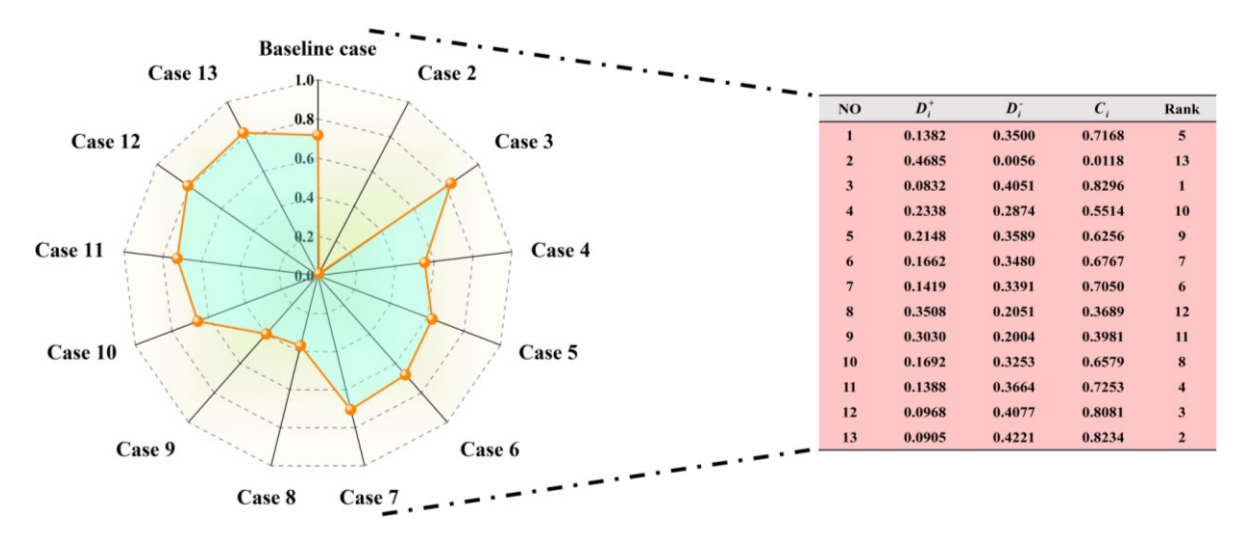


Fig. 19 Radar chart visualization of performance metrics and comprehensive assessment results for the TSTPG system.

5. Conclusions

This study has systematically studied the application of diatomite-modified calciumbased materials in solar thermochemical energy storage from three aspects: reaction kinetics, reactor exothermic process, and system integration optimization. The main conclusions are drawn as follows:

- 1. It revealed the effect of diatomite doping on the exothermic reaction mechanism of calcium-based materials. Using C-R integral method and ABSW differential method, kinetic models before and after modification were established. The results showed that pure calciumbased materials obeyed the A3 model, but it was reduced to the D2 model after diatomite modification. The introduction of diatomite reduced the activation energy (from 74.74 kJ/mol to 68.22 kJ/mol) and increased the pre-exponential factor (from 162.88 s⁻¹ to 192.50 s⁻¹).
- 2. Regarding the reactor exothermic process, it systematically analyzed the evolution patterns of temperature field, reaction extent and pressure field in the packed bed reactor. It was found that the optimal reaction temperature was 650 K, and reducing porosity from 0.6 to 0.3 significantly extended the exothermic time along with the CO₂ flow rate showing optimal effects at 15 L/min. Additionally, it proposed an optimized design incorporating intermediate air channels, which reduced the reaction time by 28.57%. It also showed that increasing the reactant thermal conductivity can accelerate the reaction rate and heat transfer efficiency.
 - 3. For the first time, it systematically investigated the impact on TSTPG system from

the perspective of reactor exothermic characteristics. Through the 4E analysis framework and multi-dimensional evaluation system based on entropy-TOPSIS method, it was found that economics (31.50%) and exergy efficiency (22.39%) are the most important factors in system evaluation. Under optimal conditions (650 K), the system achieved a power generation capacity of 23.13 MW along with system energy and exergy efficiencies respectively reaching 56.86% and 49.06% and an annual total cost of 4.11 m\$/year.

This study has explored the performance optimization pathways for thermochemical energy storage systems from the perspective of reactor exothermic characteristics, but challenges remain in engineering practice. Future works can be focused on optimizing the reactor structure design and operational strategies, deeply exploring the correlation between the heat and mass transfer mechanisms and system dynamic response characteristics. Meanwhile, there is an urgent need to establish a more comprehensive system performance evaluation framework to achieve coordinated optimization of energy storage and power generation processes. The development of these works will provide foundations and engineering support for the large-scale application of thermochemical energy storage technology, promoting renewable energy to play an important role in energy transition.

Nomenclature

Latin symbols					
A	Pre-exponential [s ⁻¹]	μ	Dynamic viscosity [Pa·s]		
С	Reactant molar concentration [mol·m ⁻³]	ξ	Convective heat transfer coefficient [W/m²·K		
Cp	Heat capacity [J·kg ⁻¹ ·K ⁻¹]	σ	Stefan-Boltzmann constant [W/m ² ·K ⁴]		
D	Diameter [mm]	α	Absorption coefficient		
H	Height of reactor [mm]	ϕ	Maintenance factor		
$egin{array}{c} E \ k \end{array}$	Activation energy [$J \cdot mol^{-1}$] Permeability [m ²]	Subscripts			
f	Effective reaction ratio	eff	Effective		
K	Reaction rate coefficient [s ⁻¹]	eq	Equilibrium		
M	Mole mass [kg·mol ⁻¹]	solid	Solid reactant and product		
p	Pressure [Pa]	ini	Initial value		
R_g	Mole gas constant $[J \cdot mol^{-1} \cdot K^{-1}]$	CaCO ₃	Reactant CaCO ₃		
T	Temperature [K]	CaO	Reactant CaO		
u	Velocity [m·s ⁻¹]	elec	Electrical		
X	Reaction extent	rec	receiver		
$Q_{ m m}$	Mass source [kg·m ⁻³ ·s ⁻¹]	t	turbine		
T_{eq}	Temperature at equilibrium state [K]	c	compressor		
C	Cost [\$]	Abbreviations			
C _{elec, peak}	Peak electricity prices [\$/kWh]	TCES	Thermochemical energy storage		
C _{elec,off-peak}	Off-peak electricity prices [\$/kWh]	TSTPG	Thermochemical solar thermal power generation system		
&	Heat transfer rate [MW]	HTF	Heat transfer fluid		
EX	Exergy flow rate [MW]	CSP	Concentrating solar power		
n&	Mass flow rate [kg/s]	DNI	Direct normal irradiance [W/m²]		
V	Volume [m³]	HEX	Heat exchanger		
<i>1</i> 16&	Power [MW]	SPT	Solar power tower		
Greek symbol:	Greek symbols		Annual total profit		
\mathcal{E}	Porosity of reactant	CRF	Capital recovery factor		
ρ		DDD	D : 1 1 : 1		
	Density [kg⋅m ⁻³]	DPP	Dynamic payback period		
λ	Density [kg·m ⁻³] Thermal conductivity [W·m ⁻¹ ·K ⁻¹]	DPP NPV	Net Present Value		

CRediT authorship contribution statement

Jianing Chen: Conceptualization, Methodology, Software, Writing - original

- 769 manuscript. **Xueming Yang:** Funding acquisition, Writing Reviewing and Editing. **Jie Cui:**
- 770 Conceptualization, Methodology, Software. Yinqiao Huo: Formal analysis, Software.
- Jianfei Xie: Investigation, Writing review & editing.

Declaration of Competing Interest

- The authors whose names are listed immediately below certify that they have NO affiliations with or involvement in any organization or entity with any financial interest (such as honoraria; educational grants; participation in speakers' bureaus; membership, employment, consultancies, stock ownership, or other equity interest; and expert testimony or patent-licensing arrangements), or non-financial interest (such as personal or professional relationships, affiliations, knowledge or beliefs) in the subject matter or materials discussed
- in this manuscript.

772

780

785

789 790

Acknowledgements

- 781 This research was supported by the National Natural Science Foundation of China
- (Grant No. 52076080). This work was carried out at Shanxi Supercomputing Center of China,
- and the simulations were performed on TianHe-2. The author thanks the editors and reviewers
- for their careful review and many constructive suggestions on the manuscript.

Funding information

- This research was supported by the National Natural Science Foundation of China
- 787 (Grant No. 52076080). This work was carried out at Shanxi Supercomputing Center of China,
- and the simulations were performed upon TianHe-2.

References:

- 791 [1] Z. Su, L. Yang, H. Wang, J. Song, W. Jiang, S. Liu, et al. 6E analysis and particle swarm optimization of a
- 792 novel ultra-high temperature solar cogeneration system fusing thermochemical energy storage and multistage
- 793 direct heat transfer. Energy Conversion and Management. 317 (2024) 118867.
- 794 [2] X. Tian, S. Guo, X. Lv, S. Lin, C.-Y. Zhao. Progress in multiscale research on calcium-looping for
- thermochemical energy storage: From materials to systems. Progress in Energy and Combustion Science. 106
- 796 (2025) 101194.
- 797 [3] X. Yang, H. Zhao, M. Zhang, C. Ji, J. Xie. Performance comparison of CSP system with different heat
- transfer and storage fluids at multi-time scales by means of system advisor model. Solar Energy Materials and
- 799 Solar Cells. 269 (2024) 112765.
- 800 [4] J.I. Burgaleta, S. Arias, D. Ramirez. Gemasolar, the first tower thermosolar commercial plant with molten
- salt storage. SolarPACES, Granada, Spain. (2011) 20-3.
- [5] L. Yao, Z. Guan, Y. Wang, H. Hui, S. Luo, C. Jia, et al. Evaluating the feasibility of concentrated solar power

- as a replacement for coal-fired power in China: A comprehensive comparative analysis. Applied Energy. 377
- 804 (2025) 124396.
- 805 [6] S.K. Gupta, Y. Mao. A review on molten salt synthesis of metal oxide nanomaterials: Status, opportunity,
- and challenge. Progress in Materials Science. 117 (2021) 100734.
- 807 [7] J. Chen, H. Su, H. Sun, J. Xie, X. Yang. Kinetic investigation and numerical simulation of reactor with
- prepared diatomite/CaCO₃ for high-temperature thermal energy storage application. Journal of Energy Storage.
- 809 96 (2024) 112694.
- [8] J. Chen, X. Yang, H. Su, J. Cui, J. Xie. Evaluating and enhancing heat storage in a Ca(OH)₂/CaO shell-tube
- 811 reactor: A numerical study on key factors and performance optimization. Energy. 309 (2024) 133161.
- 812 [9] X. Tian, S. Guo, S. Lin, J. Yan, S. Ju, C. Zhao. Exploring synergistic sintering factors and nanopore
- regeneration of calcium-based thermochemical energy storage materials. Solar Energy Materials and Solar Cells.
- 814 263 (2023) 112593.
- [10] X. Yang, H. Su, W. Liang, J. Chen, J. Xie. Numerical study of Mg(OH)₂/MgO thermochemical heat storage
- reactor coupled with parabolic dish solar system. Applied Thermal Engineering. (2024) 125128.
- 817 [11] D. Zhang, X. Yang, H. Li, Z. Jia, S. Zhang, S. Tang, et al. 4E analysis and parameter study of a solar-
- thermochemical energy storage CCHP system. Energy Conversion and Management. 301 (2024) 118002.
- 819 [12] M. Benitez-Guerrero, J.M. Valverde, P.E. Sanchez-Jimenez, A. Perejon, L.A. Perez-Maqueda. Calcium-
- 820 Looping performance of mechanically modified Al₂O₃-CaO composites for energy storage and CO₂ capture.
- 821 Chemical Engineering Journal. 334 (2018) 2343-55.
- 822 [13] A.A. Khosa, C. Zhao. Heat storage and release performance analysis of CaCO₃/CaO thermal energy storage
- system after doping nano silica. Solar Energy. 188 (2019) 619-30.
- 824 [14] T. Xu, X. Tian, A. Khosa, J. Yan, Q. Ye, C. Zhao. Reaction performance of CaCO₃/CaO thermochemical
- energy storage with TiO₂ dopant and experimental study in a fixed-bed reactor. Energy. 236 (2021) 121451.
- 826 [15] K. Wang, F. Gu, P.T. Clough, P. Zhao, E.J. Anthony. Porous MgO-stabilized CaO-based powders/pellets
- via a citric acid-based carbon template for thermochemical energy storage in concentrated solar power plants.
- 828 Chemical Engineering Journal. 390 (2020) 124163.
- 829 [16] Y. Deng, Z. Zhu, Z. Liu, W. Li, W. Zhang, B. Yu. Study on coupling characteristics of thermal-fluid-
- chemical multi-physics field in CaCO₃/CaO thermochemical exothermic reactor. Chemical Engineering Science.
- 831 299 (2024) 120453.
- 832 [17] X. Tian, S. Guo, L. Jiang, S. Lin, J. Yan, C. Zhao. Integrated operation and efficiency analysis of
- 833 CaCO₃/CaO in a fixed-bed reactor for thermochemical energy storage. Energy. 294 (2024) 130867.
- 834 [18] R. Barker. The reactivity of calcium oxide towards carbon dioxide and its use for energy storage. Journal
- of Applied Chemistry and Biotechnology. 24 (1974) 221-7.
- 836 [19] X. Chen, X. Jin, X. Ling, Y. Wang. Exergy analysis of concentrated solar power plants with thermochemical
- energy storage based on calcium looping. ACS Sustainable Chemistry & Engineering. 8 (2020) 7928-41.
- 838 [20] C. Ortiz, R. Chacartegui, J. Valverde, A. Carro, C. Tejada, J. Valverde. Increasing the solar share in
- combined cycles through thermochemical energy storage. Energy Conversion and Management. 229 (2021)
- 840 113730.
- 841 [21] M. Sattar, A. Rehman, N. Ahmad, A. Mohammad, A.A. Al Ahmadi, N. Ullah. Performance analysis and
- optimization of a cooling system for hybrid solar panels based on climatic conditions of Islamabad, Pakistan.
- 843 Energies. 15 (2022) 6278.
- 844 [22] A.A. Sher, N. Ahmad, M. Sattar, U. Ghafoor, U.H. Shah. Effect of various dusts and humidity on the
- performance of renewable energy modules. Energies. 16 (2023) 4857.
- 846 [23] S. Vyazovkin, A.K. Burnham, J.M. Criado, L.A. Pérez-Maqueda, C. Popescu, N. Sbirrazzuoli. ICTAC
- 847 Kinetics Committee recommendations for performing kinetic computations on thermal analysis data.

- 848 Thermochimica acta. 520 (2011) 1-19.
- 849 [24] D.K. Lee. An apparent kinetic model for the carbonation of calcium oxide by carbon dioxide. Chemical
- 850 Engineering Journal. 100 (2004) 71-7.
- 851 [25] P. Schmidt, M. Bouché, M. Linder, A. Wörner. Pilot plant development of high temperature
- 852 thermochemical heat storage. Proceedings of 12th Int Conference on Energy Storage (Innostock), Lleida,
- 853 Spain2012.
- 854 [26] A. Bejan. Heat Transfer Handbook. John Wiley and Sons, Inc2003.
- 855 [27] J. Holman. Heat Transfer 10th edition McGraw-Hill Book Co. New York, NY (10020). 521-67.
- 856 [28] J. Wang, Z. Lu, M. Li, N. Lior, W. Li. Energy, exergy, exergoeconomic and environmental (4E) analysis of
- a distributed generation solar-assisted CCHP (combined cooling, heating and power) gas turbine system. Energy.
- 858 175 (2019) 1246-58.
- 859 [29] Y. Cao, H. Habibi, M. Zoghi, A. Raise. Waste heat recovery of a combined regenerative gas turbine-
- 860 recompression supercritical CO₂ Brayton cycle driven by a hybrid solar-biomass heat source for multi-
- generation purpose: 4E analysis and parametric study. Energy. 236 (2021) 121432.
- 862 [30] M. Atif, F.A. Al-Sulaiman. Energy and exergy analyses of solar tower power plant driven supercritical
- carbon dioxide recompression cycles for six different locations. Renewable and Sustainable Energy Reviews.
- 864 68 (2017) 153-67.
- 865 [31] H. Guo, Y. Xu, Y. Zhang, Q. Liang, H. Tang, X. Zhang, et al. Off-design performance and an optimal
- operation strategy for the multistage compression process in adiabatic compressed air energy storage systems.
- Applied Thermal Engineering. 149 (2019) 262-74.
- 868 [32] T. Ouyang, P. Qin, S. Xie, X. Tan, M. Pan. Flexible dispatch strategy of purchasing-selling electricity for
- coal-fired power plant based on compressed air energy storage. Energy. 267 (2023) 126578.
- 870 [33] L. Chen, L. Zhang, Y. Wang, M. Xie, H. Yang, K. Ye, et al. Design and performance evaluation of a novel
- 871 system integrating Water-based carbon capture with adiabatic compressed air energy storage. Energy
- 872 Conversion and Management. 276 (2023) 116583.
- 873 [34] W. Wu, S. Xie, J. Tan, T. Ouyang. An integrated design of LNG cold energy recovery for supply demand
- balance using energy storage devices. Renewable Energy. 183 (2022) 830-48.
- 875 [35] S.B. Mousavi, M. Adib, M. Soltani, A.R. Razmi, J. Nathwani. Transient thermodynamic modeling and
- 876 economic analysis of an adiabatic compressed air energy storage (A-CAES) based on cascade packed bed
- thermal energy storage with encapsulated phase change materials. Energy conversion and management. 243
- 878 (2021) 114379.
- 879 [36] Q. Wang, L. Duan, Z. Lu, N. Zheng. Thermodynamic and economic analysis of a multi-energy
- 880 complementary distributed cchp system coupled with solar thermochemistry and active energy storage
- regulation process. Energy Conversion and Management. 292 (2023) 117429.
- 882 [37] M. Shamoushaki, D. Fiaschi, G. Manfrida, L. Talluri. Energy, exergy, economic and environmental (4E)
- analyses of a geothermal power plant with NCGs reinjection. Energy. 244 (2022) 122678.
- 884 [38] D. Zhang, C. Fang, X. Qin, H. Li, H. Liu, X. Wu. Performance study of transcritical CO2 heat pump
- 885 integrated with ejector and latent thermal energy storage for space heating. Energy Conversion and Management.
- 886 268 (2022) 115979.
- 887 [39] X. Han, H. Xu, C. Zhao. Design and performance evaluation of multi-layered reactor for calcium-based
- thermochemical heat storage with multi-physics coupling. Renewable Energy. 195 (2022) 1324-40.
- [40] R. Han, J. Gao, S. Wei, Y. Su, F. Sun, G. Zhao, et al. Strongly coupled calcium carbonate/antioxidative
- graphite nanosheets composites with high cycling stability for thermochemical energy storage. Applied Energy.
- 891 231 (2018) 412-22.